On the nonlinear relationship between wall shear stress topology and multi-directionality in coronary atherosclerosis

Harry J. Carpenter [a,*], Mergen H. Ghayesh [a,*], Anthony C. Zander [a], Peter J. Psaltis [b,c,d]

[a] School of Mechanical Engineering, University of Adelaide, Adelaide, South Australia 5005, Australia
[b] Vascular Research Centre, Lifelong Health Theme, South Australian Health and Medical Research Institute (SAHMRI), Adelaide, South Australia 5000, Australia
[c] Adelaide Medical School, University of Adelaide, Adelaide, South Australia 5005, Australia
[d] Department of Cardiology, Central Adelaide Local Health Network, Adelaide, South Australia 5000, Australia

ARTICLE INFO

ABSTRACT

Background and Objective: In this paper we investigate twelve multi-directional/topological wall shear stress (WSS) derived metrics and their relationships with the formation of coronary plaques in both computational fluid dynamics (CFD) and dynamic fluid-structure interaction (FSI) frameworks. While low WSS is one of the most established biomechanical markers associated with coronary atherosclerosis progression, alone it is limited. Multi-directional and topological WSS derived metrics have been shown to be important in atherosclerosis related mechanotransduction and near-wall transport processes. However, the relationships between these twelve WSS metrics and the influence of both FSI simulations and coronary dynamics is understudied.

Methods: We first investigate the relationships between these twelve WSS derived metrics, stenosis percentage and lesion length through a parametric, transient CFD study. Secondly, we extend the parametric study to FSI, both with and without the addition of coronary dynamics, and assess their correlations. Finally, we present the case of a patient who underwent invasive coronary angiography and optical coherence tomography imaging at two time points 18 months apart. Associations between each of the twelve WSS derived metrics in CFD, static FSI and dynamic FSI simulations were assessed against areas of positive/negative vessel remodelling, and changes in plaque morphology.

Results: 22–32% stenosis was the threshold beyond which adverse multi-directional/topological WSS results. Each metric produced a different relationship with changing stenoses and lesion length. Transient haemodynamics was impacted by coronary dynamics, with the topological shear variation index suppressed by up to 94%. These changes appear more critical at smaller stenosis levels, suggesting coronary dynamics could play a role in the earlier stages of atherosclerosis development. In the patient case, both dynamics and FSI vs CFD changes altered associations with measured changes in plaque morphology. An appendix of the linear fits between the various FSI- and CFD-based simulations is provided to assist in scaling CFD-based results to resemble the compliant walled characteristics of FSI more accurately.

Conclusions: These results highlight the potential for coronary dynamics to alter multi-directional/topological WSS metrics which could impact associations with changes in coronary atherosclerosis over time. These results warrant further investigation in a wider range of morphological settings and longitudinal cohort studies in the future.

1. Introduction

Coronary atherosclerosis burdens society through significant mortality, morbidity, and economic losses [1]. Despite a decrease in the incidence of acute myocardial infarction (AMI) driven by coronary atherosclerosis around the developed world over the past two decades, non-ST-elevation myocardial infarction (NSTEMI) is increasing [2]. This has important long-term implications for patients and the wider healthcare sector as NSTEMI is associated with worsening outcomes and long-term mortality when coupled with multivessel disease (MVD) [3–5]. Optimal treatment options for MVD in the setting of NSTEMI are also not well defined, and multivessel revascularisation by percutaneous coronary inter-

* Corresponding author.
E-mail addresses: harry.carpenter@adelaide.edu.au (H.J. Carpenter), mergen.ghayesh@adelaide.edu.au (M.H. Ghayesh).

vention (PCI) remains relatively uncommon in real-world clinical practice [6]. This partly stems from an inability to predict which non-culprit lesions in patients with MVD will ultimately cause ischaemia through progression and/or destabilisation over time [7,8]. To improve patient outcomes there is a need to assist clinicians to more accurately predict which patients and plaques have an increased likelihood of future ischaemic events [6]. This could assist with personalised decision making, such as by guiding the use of more intensive pharmacotherapy or by guiding the use of non-culprit PCI, to turn the tide on these worsening outcomes.

Biomechanical simulation has emerged as a useful tool to analyse the unique mechanics that contribute to disease progression throughout the coronary vasculature [9]. Three primary approaches covering fluid mechanics and computational fluid dynamics (CFD), structural mechanics (both static and transient) and fully coupled fluid-structure interaction (FSI) have been applied to study how biomechanical markers contribute to atherosclerotic lesion formation, progression and destabilisation over time [10]. Of these, wall shear stress (WSS) is the most established marker. There exists a broad consensus that WSS magnitude associates with the deposition of atherogenic biomarkers and altered mechanotransduction, contributing to endothelial cell dysfunction and different signalling pathways producing inflammatory responses [11–15]. While this has led to WSS associating with both lesion progression and changes in plaque composition, WSS magnitude alone has only been able to provide incremental improvements to the stratification of patients risks [16–18]. However, the relationship between WSS and atherogenesis is not straightforward.

Multi-directional WSS markers are now evolving as potentially more useful in understanding disease progression than WSS magnitude alone. The oscillatory shear index (OSI) is the most established of these markers, quantifying the degree of flow reversal at the lumen wall, and has been suggested as a mechanism that contributes to atherogenic endothelial dysfunction [19,20]. However, emerging WSS markers can now quantify the directional characteristics of complex flow conditions in greater detail. Transverse WSS (TrWSS) and its normalised version, the cross-flow index (CFI), make use of the lumen surface characteristics to better quantify this multi-directionality [21,22]. These markers in combination with WSS magnitude have been shown to associate with the development of thin-capped fibroatheroma (TCFA), a high-risk plaque phenotype, with the speed of lesion development correlated with both low WSS magnitude and high multi-directional WSS [23]. Similarly, secondary WSS (WSSsec), the WSS component acting in the circumferential direction of the lumen surface, has been shown to associate with atheroprotective helical flow properties, allowing this multi-directional WSS marker to better present information on intraluminal flow characteristics [24,25].

A more recent concept is that of WSS topology, first introduced through Lagrangian approaches to quantify prominent near-wall flow features and species surface transport [26–28]. By leveraging the near wall features of blood flow to develop a WSS exposure time metric it was demonstrated that this approach can far more accurately characterise the surface concentrations computed from advection-diffusion equations than multi-directional measures such as relative residence time (RRT) [29]. Furthermore, the role of critical/fixed points within the near-wall velocity and WSS vector field, points indicative of flow separation and impingement, have also been linked to surface biochemical transport and impaired endothelial cell function, alignment, and migration [30–32]. In order to provide a simpler, but mathematically less rigorous method for WSS topology analysis, a Eulerian approach rooted in volume contraction theory was proposed to determine WSS divergence and its topological shear variation index (TSVI); its variation over the cardiac cycle [33,34]. The physiological significance of these metrics has also recently been demonstrated, with associations between WSS divergence contraction/expansion regions and worsening outcomes following carotid endarterectomy [33,35] and association between amplified TSVI and coronary wall thickening over time [36]. Very recently TSVI was also demonstrated to be superior to WSS magnitude alone in predicting both NSTEMI and STEMI at 5-year follow up [37]. However, all these studies still assume rigid-walled CFD simulations.

FSI could improve our ability to describe the complex flow characteristics in the coronary vasculature by including the dynamic and compliant properties of the artery wall [38–40]. However, the debate between using CFD or FSI simulations in coronary biomechanics is still ongoing, with arguments for and against each approach often focused on the differences in WSS magnitude [40–42]. To date, no approach has investigated how multi-directional/topological WSS measures are related within and between CFD and FSI simulations, nor how coronary dynamics and wall compliance could impact these relationships and their subsequent associations with changes in the coronary vasculature. Here we address these gaps as follows: (1) First, we present a parametric study on the effect of stenosis percentage and lesion length on twelve multi-directional/topological WSS measures to investigate their relationships. (2) We then investigate the inter- and intraclass correlations between these WSS metrics in CFD- and FSI-based simulations, extending the application of a number of these metrics to FSI simulations for the first time. (3) We extend the FSI-based correlations to study the impact of coronary dynamics on these metrics. (4) Finally, we present a patient-specific case and show how discrepancies between varying simulations and their dynamic boundary conditions could impact associations with coronary atherosclerosis. An appendix of linear correlations is also provided which could prove useful in scaling CFD-based results to resemble more closely the compliant-walled characteristics of FSI.

2. Methods

2.1. Idealised, parametric geometry

An idealised atherosclerotic left anterior descending coronary artery was developed based on the geometry presented in [42] to validate the modelling process and parametrically analyse the impact of stenosis severity, lesion length, FSI simulation and artery dynamics on WSS vector field topology (Fig. 1). These idealised simulations present a reproducible benchmark for multi-directional/topological metrics and their relationships for future computational and experimental fluid dynamics studies. A fibrous cap thickness (FCT) of 50 μm overlying a lipid pool was held consistent in all simulations, while the artery centreline coordinates were varied with stenosis percentage, calculated as the ratio of the difference between the minimum lumen radius and the normal lumen radius (1.5 mm in this case) over the normal lumen radius. Stenosis percentages from 0 to 54% were studied, using a constant lesion length of 18 mm as in [42], as well as lesion lengths ranging from 6 to 18 mm. These are often angiographically visible factors which could suggest the need for intervention and associate with the functional severity of the lesion [43–45] and have been identified as important factors in previous fluid dynamics studies [46–49]. Furthermore, the eccentric nature of the vessel was kept constant due to the added pressure load placed on the proximal region (hence suggesting a more vulnerable lesion) [49]. The change in lesion length was studied for a constant 43% stenosis, as this stenosis percentage has long been suggested as a critical threshold for plaque rupture [50]. These morphological parameters are by no means an exhaustive assessment of atherosclerotic lesion anatomy and future studies should investigate a larger range of geometries.
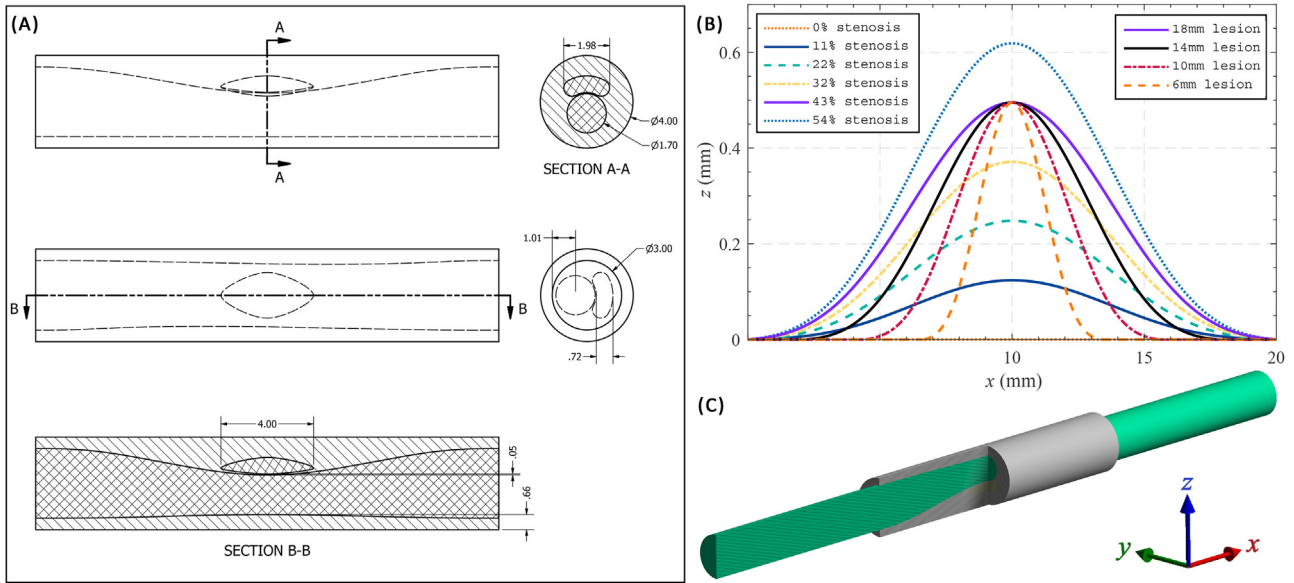
Fig. 1. Schematic of the model geometry. (A) Dimensions for the 43% stenosis model shown in mm. (B) Centreline coordinates of the nine different geometries. (C) Render of the proposed geometry with inlet and outer fluid regions (highlighted) extended to remove the influence of fluid boundary conditions and the cut-out visualising stenosis and plaque.

Table 1
Material property coefficients for the orthotropic hyperelastic material model (artery wall).

a_1(MPa)	a_2(MPa)	a_3(MPa)	b_{1-3}(MPa)	c_1(MPa)	c_2(MPa)	e_1(MPa)	e_2(MPa)	d(MPa^{-1})
2.63e-2	−1.04e-1	1.22	0	1.10e-1	2.37e1	4.62e-3	8.97	2.00

2.2. Artery/structural material properties

The artery wall was modelled as an orthotropic hyperelastic structure while the lipid pool was modelled as a three-parameter, isotropic Mooney-Rivlin model, consistent with previous investigations. The orthotropic hyperelastic strain energy density function was applied from ANSYS' special hyperelasticity functions, described by [51]

$$W\left(\bar{C}, A \otimes A, B \otimes B\right) = \sum_{i=1}^{3} a_i\left(\bar{I}_1 - 3\right)^i + \sum_{j=1}^{3} b_j\left(\bar{I}_2 - 3\right)^j$$
$$+ \frac{c_1}{2c_2}\left\{\exp\left[c_2\left(\bar{I}_4 - 1\right)^2\right] - 1\right\}$$
$$+ \frac{e_1}{2e_2}\left\{\exp\left[e_2\left(\bar{I}_6 - 1\right)^2\right] - 1\right\}$$
$$+ \frac{1}{d}(J - 1)^2, \tag{1}$$

where $\bar{I}_{1,2,4,6}$ are invariants of the right Cauchy Green tensor and a_{1-3}, b_j, $c_{1,2}$, d and $e_{1,2}$ are material coefficients derived by fitting against data presented for coronary artery layers in [52]. The fitted coefficients are highlighted in Table 1. Note a small amount of artificial compressibility was introduced to assist in overcoming volumetric locking in the finite element formulation. For simplicity in the curve fitting process, we use the principal axial and circumferential directions as the two-fibre directions, described in Eq. (2), and fitted the radial direction based on the anisotropic model results presented in [53]. This assisted in maintaining Drucker stability during the nonlinear curve fit and stability under three-dimensional stress states in the finite element simulations.

$$Artery\begin{cases} A = \langle 1, 0, 0 \rangle \\ B = \langle 0, 1, 0 \rangle \end{cases}, \tag{2}$$

Table 2
Hyperelastic coefficients for the 3-paramater Mooney-Rivlin model (Lipid).

C_{10}(MPa)	C_{01}(MPa)	C_{11}(MPa)
5.01e-3	−1.00e-3	7.00e-2

The lipid was modelled as an isotropic, three-parameter Mooney-Rivlin model [54,55] described by

$$W = c_{10}(\bar{I}_1 - 3) + c_{01}(\bar{I}_2 - 3) + c_{11}(\bar{I}_1 - 3)(\bar{I}_2 - 3), \tag{3}$$

where c_{10}, c_{01} and c_{11} are coefficients determined by fitting to experimental data from [56] and the compressibility term was omitted as the lipid is modelled as an incompressible material. The coefficients are outlined in Table 2. Both the artery and lipid had a constant density of 1000 kg/m^3. The material responses are described in Fig. 2, with the axial and circumferential ranges highlighting the significant variability that is present in the coronary vasculature. Due to this variability, and our use of tissue properties that could be argued as more compliant than atherosclerotic tissue, results can be considered an upper bound on the variability between CFD and FSI. Further work should consider this important factor and could also investigate how the stiffening of vessels with age/disease change the importance of considering dynamic/coupling factors (i.e., could younger and healthier vessels be impacted more significantly by dynamics and, if so, does this mean coronary dynamics is a more significant factor in the developmental stages of disease?) Furthermore, future simulation capability can be improved with the development of user-programmable features to extend ANSYS' capabilities to include Holzapfel-Gasser-Odgen models which more accurately define fibre orientation [57].
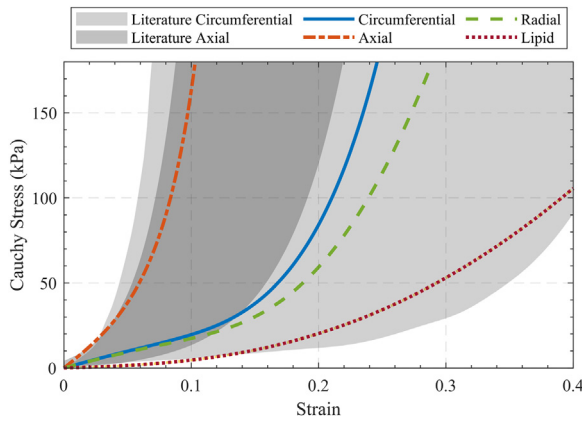
Fig. 2. Stress-strain relationships for the fitted orthotropic hyperelastic artery and three-parameter Mooney-Rivlin lipid compared to experimental ranges for both the circumferential and axial directions previously presented for the intima layer in the literature.

2.3. Blood/fluid properties

Blood flow was modelled as a homogenous, incompressible, fully developed, unsteady and non-Newtonian fluid. Consistent with accepted assumptions, we apply a no-slip boundary condition at vessel walls. However, it should be noted that coronary vessels are in fact rough surfaces which could suggest a slip boundary condition as the most realistic approach [58–60]. The fully developed, transient inlet velocity profile and the characteristic out-of-phase pressure outlet are described in Fig. 3. A fully developed inlet profile coupled with the extended inlet/outlet regions was deemed sufficient as previous studies suggested the inlet flow profile only impacts the very proximal haemodynamics in coronary settings [61,62]. Blood velocity and pressure profiles were adapted from the literature and were characterised by a 20-term Fourier series [63]. The higher order Fourier series was used to capture the subtle secondary peaks caused by the backward propagating pressure waves between cardiac phases in the coronary vasculature which could impact WSS topology, shown inset in Fig. 3. Non-Newtonian blood viscosity was modelled using the Carreau model, which best captures the shear-thinning nature of blood and is described by [64],

$$\mu = \mu_\infty + (\mu_0 - \mu_\infty)\left[1 + (\lambda\dot{\gamma})^2\right]^{0.5(n-1)}, \tag{4}$$

where μ_0 and μ_∞ are the zero and infinite shear viscosity limits, respectively, λ is a time constant, n is the power law coefficient and γ is the fluid strain rate whose coefficients are: $\mu_\infty = 0.056$ Pa.s; $\mu_0 = 0.00345$ Pa.s; $\lambda = 3.313$ s; $n = 0.3568$ [64]; and the fluid density was set to 1050 kg/m³. The k-omega shear stress transport turbulence model was used to capture potential transitional-turbulent recirculation regions downstream of the increasing stenosis and allowed combination of the far-field, free stream independence of the k-epsilon model with the accuracy of the near-wall k-omega formulation [65]. This was motivated by previous studies which demonstrated that WSS and OSI can vary by more than 10% distal to lesions with stenoses levels greater than 50% when using turbulence modelling [66–69] and is consistent with previous studies that made use of this model to reduce computation cost compared to Reynolds stress or Large Eddy simulation models while producing a flow environment downstream of a stenosis that more accurately matched experimental measurements compared to other approaches [70–72]. While other studies also applied turbulence modelling, citing stenosis levels and bifurcation related haemodynamics, it should be noted that this introduces further assumptions to the simulations [38,73,74]. As coronary flow can often be described as transitional rather than fully turbulent, it is generally

accepted that the laminar flow condition in conjunction with an appropriately fine mesh is sufficient to decompose this transitional region.

2.4. Coronary dynamics

An idealised dynamical profile was developed based on previous investigations tracking cardiac motion [75,76]. The profile, shown in Fig. 4, was applied to the artery inlet and outlet, with a 5% axial compression included to capture the unique compressive effects on the coronary vasculature, which were shown to impact local coronary flow conditions [77]. To assess the impact of dynamical direction, the simulation results using the displacement profile were compared to results from the same profile with inverted direction. The coronary centrelines, described in Section 2.1, were updated at each time step by mapping centreline points to nodal coordinates in the undeformed condition and then tracking the deformation of the associated nodes. This allowed axial and secondary WSS to be calculated while including the dynamic interaction between the artery structure and blood flow. It should be noted that this idealised dynamic profile omits other critical factors present in normal coronary function, including vessel bending, torsion and active contraction of the media layer, of which many have been studied previously [78–81]. Here we only study the impact of idealised three-dimensional motion and its direction, not the impact of dynamic magnitude or variations in the transient profile. Patient-to-patient variations throughout the vasculature can be significant, with notable differences between the major epicardial vessels [38]. This makes generalising results from this work difficult. This limitation should be considered, with future work needed to investigate how these factors could amplify or suppress the results we present.

2.5. Discretisation and numerical scheme

The numerical models were solved in the commercial software ANSYS (version 2020R2, Cannonsburg, PA, US), by means of the finite element and finite volume methods for the structural and fluid-based components, respectively. The two-way, transient simulation was temporally discretised into 6 ms time steps (150 time steps per 0.9s cardiac cycle) with up to 12 system coupling iterations allowable per time step, sufficient for convergence. The structural component made use of nonlinear 10-node tetrahedral elements with a Lagrangian mixed displacement-hydrostatic pressure element formulation due to the near incompressibility of the artery and incompressible lipid. Topology between the artery and lipid was shared to remove the need to model contact regions. A sparse direct solver was used for robustness due to the orthotropic nonlinear simulation properties with a maximum of 50 allowable structural iterations per system coupling step. The fluid domain was discretised with four-node linear tetrahedral elements and an allowable 400 iterations per system coupling step. Second order temporal and spatial discretisation schemes were used for all simulations and spring-based dynamic mesh smoothing was applied (but not remeshing) to allow the domain to deform while maintaining consistent element order and connectivity matrices throughout the simulation. This allowed node based postprocessing to be carried out (see Section 2.6-2.7).

Mesh independence tests were carried out for both domains by varying the element size and the minimum allowable number of elements across gaps (such as the fibrous cap) in the structural domain and the wall element size in the fluid domain, as described in Table 3. Variation of less than one percent was considered acceptable for mesh independence, with the fine mesh chosen for subsequent simulations. The simulation was validated against data presented in the literature for a 43% stenosis, with results shown
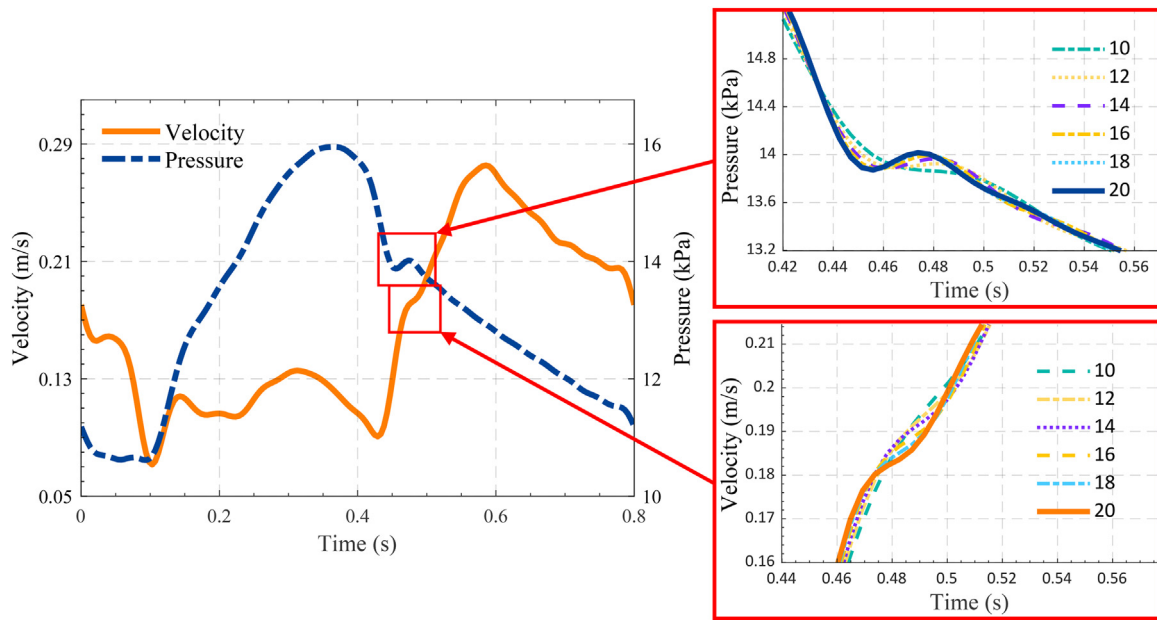
Fig. 3. Blood velocity and pressure profiles. Inset, variations in each profile for increasing number of Fourier series terms, with 20 terms best capturing the secondary pressure pulse and velocity fluctuations.
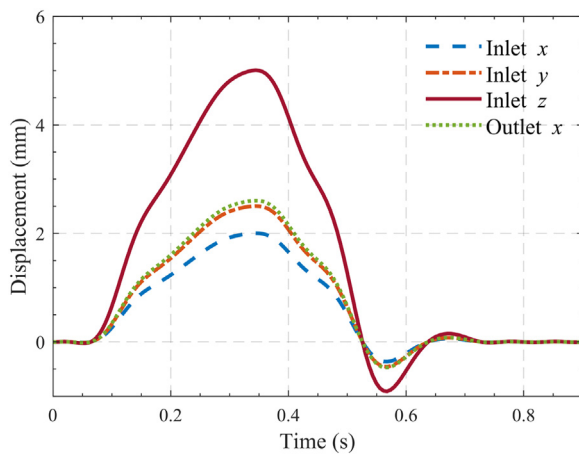

Fig. 4. Displacement boundary conditions. Transient profiles were also inverted to study the effect of displacement direction on topological results.

in Fig. 5 and showing good agreement. Discrepancies between results were likely caused by our use of a single walled model (rather than including two layers) and the use of a different hyperelastic material model. The use of higher order Fourier series for transient boundary conditions also likely contributed to this variation with the cited literature not specifically outlining how their profiles were implemented.

2.6. Multi-directional wall shear stress metrics

We first describe three established WSS measures, namely the time averaged WSS (TAWSS), oscillatory shear index (OSI) [82], and relative residence time (RRT) [83], defined in Eq. 5:

$$
\left.\begin{array}{l}
TAWSS = \frac{1}{T} \int_0^T |\boldsymbol{\tau}| dt \\
OSI = 0.5 \left(1 - \frac{\left| \int_0^T \boldsymbol{\tau} dt \right|}{\int_0^T |\boldsymbol{\tau}| dt} \right) \\
RRT = \left(\frac{1}{T} \left| \int_0^T \boldsymbol{\tau} dt \right| \right)^{-1}
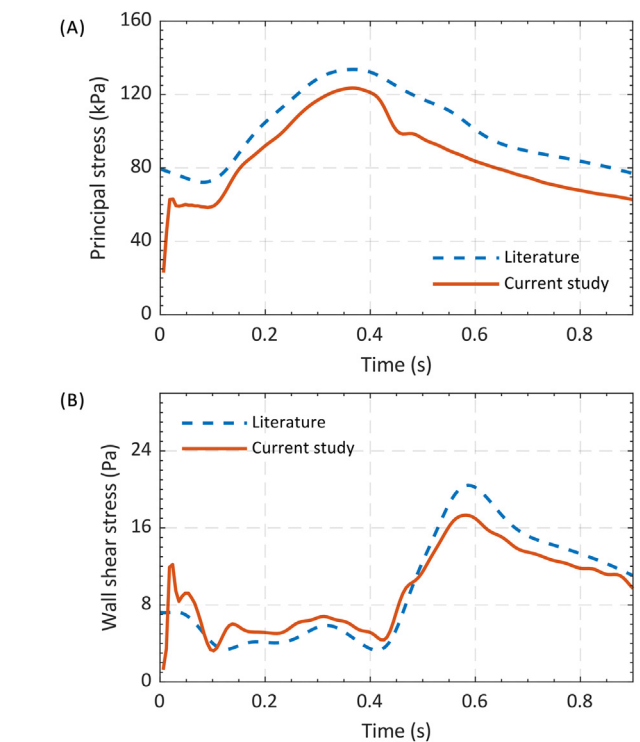\end{array}\right\}.
\tag{5}
$$

Fig. 5. Validation of the simulation method used in the current study against the literature. (A) Principal stress. (B) Wall shear stress. The results show good agreement.

Here, T is the cardiac cycle time (0.9 s in this case), $\boldsymbol{\tau}$ is the WSS vector and t is time. OSI describes the reversal of flow over the cardiac cycle and RRT combines both TAWSS and OSI to give a marker of near wall stagnation.

Cross Flow Index and Transverse WSS: The TrWSS [22], and its normalised version the CFI [21], can characterise the multi-directional nature of coronary blood flow patterns. These metrics make use of the lumen face normal properties which are updated

Table 3
Mesh independence study for the idealised case. Variation in the maximum Principal stress in both the thin fibrous cap and in the artery wall opposite the plaque were compared as well as the wall shear stress at the location of greatest lumen narrowing. Percentage variation in results is shown compared to the 'fine' mesh sizing which was used for the subsequent simulations. Results were assumed independent of mesh properties for variations of less than one percent.

Structural	Mesh Size (mm)	Minimum Elements Over Gap	Number of Elements	Maximum fibrous cap Principal Stress Variation (%)	Maximum wall Principal Stress Variation (%)
Coarse	0.15	1	432,419	5.409	3.303
Medium	0.12	2	831,994	1.864	2.904
Fine	0.10	3	1437,844	–	–
Extra Fine	0.08	4	2500,854	0.172	0.640

Fluid	Mesh Size (mm)	Wall Refinement Size (mm)	Number of Elements	Wall Shear Stress Variation (%)
Coarse	0.14	0.12	745,331	2.709
Medium	0.12	0.09	1203,122	2.238
Fine	0.10	0.06	2251,794	–
Extra Fine	0.08	0.03	5730,348	0.855

at every time step in FSI simulations due to the deforming surface. Hence, to characterise these in FSI simulations, scalar fields are first derived based on the instantaneous deformed mesh surface and then averaged over the cardiac cycle resulting in TrWSS and CFI being described by

$$\left. \begin{aligned} WSStr &= \frac{1}{T}\int_0^T \left| \boldsymbol{\tau} \cdot \left(\mathbf{n}(t) \times \frac{\int_0^T \boldsymbol{\tau}\, dt}{|\int_0^T \boldsymbol{\tau}\, dt|} \right) \right| dt \\ CFI &= \frac{1}{T}\int_0^T \left| \frac{\boldsymbol{\tau}}{|\boldsymbol{\tau}|} \cdot \left(\mathbf{n}(t) \times \frac{\int_0^T \boldsymbol{\tau}\, dt}{|\int_0^T \boldsymbol{\tau}\, dt|} \right) \right| dt \end{aligned} \right\}, \tag{6}$$

where $\mathbf{n}_\eta(t)$ is the lumen surface normal at the node associated with WSS vector, $\boldsymbol{\tau}$, at time t.

Axial and secondary WSS: Axial WSS (WSSax) and secondary WSS (WSSsec) provide directional properties of the WSS vector field based on the artery geometry [24]. WSSax is the projection of the WSS vector field along the artery centreline, $\mathbf{C}$, whilst WSSsec is the projection of the WSS vector field along the artery circumference, $\mathbf{Q}$, calculated using the vector tangent to the artery centreline, $\mathbf{R}$, that passes through the artery centreline and the lumen surface node. As with TrWSS and CFI, the artery properties are updated at every timestep to account for the deforming surface in FSI. These are described in Eq. 7.

$$\left. \begin{aligned} WSSax &= \frac{\boldsymbol{\tau}\cdot\mathbf{C}}{|\mathbf{C}|}\frac{\mathbf{C}}{|\mathbf{C}|} \\ WSSsc &= \frac{\boldsymbol{\tau}\cdot\mathbf{Q}}{|\mathbf{Q}|}\frac{\mathbf{Q}}{|\mathbf{Q}|}, \quad \mathbf{Q} = \frac{\mathbf{C}\times\mathbf{R}}{|\mathbf{C}||\mathbf{R}|} \end{aligned} \right\} \tag{7}$$

To assess the directional properties of the axial and secondary WSS measures, independent of WSS magnitude, we also investigate the normalised version of each metric by first normalising the WSS vector.

2.7. Topological wall shear stress metrics

The basis of these topological analyses is found in volume contraction theory which has been described for cardiovascular flows elsewhere [84]. A key assumption is that the normal component of near-wall velocity tends to zero, allowing the expression of near-wall velocity in terms of the traction (WSS vector) and blood viscosity. This is possible as the normal near-wall velocity component has been demonstrated as second order with respect to tangential near-wall velocity, providing little impact on further calculations [85]. Furthermore, the most significant component normal to the wall is time independent, with further transient terms arising as an order of magnitude smaller, further reducing their importance. Under the assumption of no penetration/flux through the wall, continuity of normal velocities must be maintained between the fluid and wall. As in CFD simulations the wall is rigid, the near-wall normal velocity must tend to zero, as mentioned. In deforming FSI domains, to satisfy continuity, additional normal velocity components arise [86]. Throughout the following analyses we assume that these components are negligible with respect to the tangential components, allowing extension of the Eulerian approach from [33]. This is a particularly important consideration that requires mathematical investigation moving forward, as areas of very low WSS (and hence very low near-wall tangential velocity which are biologically relevant in the natural history of atherosclerosis) could be more significantly impacted by these transient normal terms than areas of high near-wall velocity.

WSS Divergence: The divergence of the normalised WSS vector field, $\nabla \cdot \boldsymbol{\tau}/\|\boldsymbol{\tau}\|$, is analysed by adapting the method proposed in [33]. Rather than calculating the divergence based on the time averaged wall shear stress (TAWSS) vector field, which is nonsensical in FSI analyses due to the deforming mesh, we instead calculate the instantaneous scalar divergence field at every timestep with respect to current mesh coordinates and then average these scalar fields over the cardiac cycle, T, resulting in the time averaged WSS

divergence,

$$\frac{1}{T}\int_0^T \nabla \cdot \frac{\boldsymbol{\tau}(\mathbf{p},t)}{\|\boldsymbol{\tau}(\mathbf{p},t)\|}dt = \frac{1}{T}\int_0^T \nabla\tau_x(\mathbf{p},t)\cdot\hat{\mathbf{x}} + \nabla\tau_y(\mathbf{p},t)\cdot\hat{\mathbf{y}} + \nabla\tau_x(\mathbf{p},t)\cdot\hat{\mathbf{z}}dt, \tag{8}$$

at a point, $\mathbf{p}$, confined within the mesh face, η, where $\hat{\mathbf{x}}$, $\hat{\mathbf{y}}$ and $\hat{\mathbf{z}}$ are the cartesian unit vectors; τ_x, τ_y and τ_z are the x, y and z components of the WSS vector at point $\mathbf{p}$, and time $t \in [0, T]$, calculated by interpolating across the three mesh nodes on each face using piecewise linear basis functions in barycentric coordinates. By differentiating these basis functions and expressing in terms of the properties of each triangular face and the normalised WSS vector components the following is obtained

$$\left.\begin{aligned}\nabla\boldsymbol{\tau}_x(\mathbf{p},t) &= \left(\frac{\tau_{x,1}(t)}{\|\tau_1(t)\|}\right)\frac{\mathbf{n}_\eta(t)\times\mathbf{e}_{2,3}(t)}{2A_\eta(t)} + \left(\frac{\tau_{x,2}(t)}{\|\tau_2(t)\|}\right)\frac{\mathbf{n}_\eta(t)\times\mathbf{e}_{3,1}(t)}{2A_\eta(t)} + \left(\frac{\tau_{x,3}(t)}{\|\tau_3(t)\|}\right)\frac{\mathbf{n}_\eta(t)\times\mathbf{e}_{1,2}(t)}{2A_\eta(t)} \\ \nabla\boldsymbol{\tau}_y(\mathbf{p},t) &= \left(\frac{\tau_{y,1}(t)}{\|\tau_1(t)\|}\right)\frac{\mathbf{n}_\eta(t)\times\mathbf{e}_{2,3}(t)}{2A_\eta(t)} + \left(\frac{\tau_{y,2}(t)}{\|\tau_2(t)\|}\right)\frac{\mathbf{n}_\eta(t)\times\mathbf{e}_{3,1}(t)}{2A_\eta(t)} + \left(\frac{\tau_{y,3}(t)}{\|\tau_3(t)\|}\right)\frac{\mathbf{n}_\eta(t)\times\mathbf{e}_{1,2}(t)}{2A_\eta(t)} \\ \nabla\boldsymbol{\tau}_z(\mathbf{p},t) &= \left(\frac{\tau_{z,1}(t)}{\|\tau_1(t)\|}\right)\frac{\mathbf{n}_\eta(t)\times\mathbf{e}_{2,3}(t)}{2A_\eta(t)} + \left(\frac{\tau_{z,2}(t)}{\|\tau_2(t)\|}\right)\frac{\mathbf{n}_\eta(t)\times\mathbf{e}_{3,1}(t)}{2A_\eta(t)} + \left(\frac{\tau_{z,3}(t)}{\|\tau_3(t)\|}\right)\frac{\mathbf{n}_\eta(t)\times\mathbf{e}_{1,2}(t)}{2A_\eta(t)}\end{aligned}\right\}, \tag{9}$$

where $\tau_{i,j}(t)$ is the WSS at time, t, in the i direction on the jth node of the triangular face, η (linear tetrahedral elements are used resulting in three nodes per triangular surface face); $\mathbf{n}_\eta(t)$ is the normal to the face η at time t; $A_\eta(t)$ is the area of the surface face η at time t; and $\mathbf{e}_{p,q}(t)$ is the edge of the triangular face between surface nodes p and q at time t. It should be noted that this approach is *not* necessarily equivalent to the method presented in [33]. As the integral of the scalar divergence is computed using the normalised, instantaneous WSS vector field, by the triangle/integral inequality it holds that these two are not always equivalent. More importantly, this inequality is most prominent in areas of flow reversal, raising a question of the physiological significance of each approach. It should also be noted that by taking the time-average of the divergence of the normalised WSS vector field the multi-directional properties of the vector field at each time-step are captured. Taking the divergence of the normalised TAWSS vector field, as in [33], omits these subtleties. This has important implications for the interpretation of divergence and critical point locations, discussed in detail in Appendix A2.

The critical points of the normalised WSS vector field were calculated using the method proposed in [87,88], where a fixed point is contained within an element if the three determinants described in Eq. (10) all have the same sign.

$$\left.\begin{aligned}\det\left[\tau_{x\eta}, \tau_{y\eta}, \mathbf{n}_\eta\right] \\ \det\left[\tau_{y\eta}, \tau_{z\eta}, \mathbf{n}_\eta\right] \\ \det\left[\tau_{z\eta}, \tau_{x\eta}, \mathbf{n}_\eta\right]\end{aligned}\right\} \tag{10}$$

As our computation of the divergence and critical points is carried out at each time-step, we avoid the paradoxical results questioning the role of fixed/critical point locations in the TAWSS vector field that were previously highlighted in [33]. This is discussed further in Appendix A2.

To validate the developed post-processing we compare our results against benchmarking presented in [33] on a two-dimensional, linear, triangular surface mesh computed via the Delaunay triangulation of the set of discrete points, $\mathbf{P}$, where D: $\{x| -2 \le x \le 2\}$ and R: $\{y| -2 \le y \le 2\}$ for the vector field,

$$\left.\begin{aligned}\dot{x} &= x - \frac{x^3}{3} - y \\ \dot{y} &= x - 2y\end{aligned}\right\}. \tag{11}$$

The vector field with stable manifolds and the calculated divergence of the normalised vector field with critical points is shown in Fig. 6, with excellent agreement to the benchmarking presented in [33].
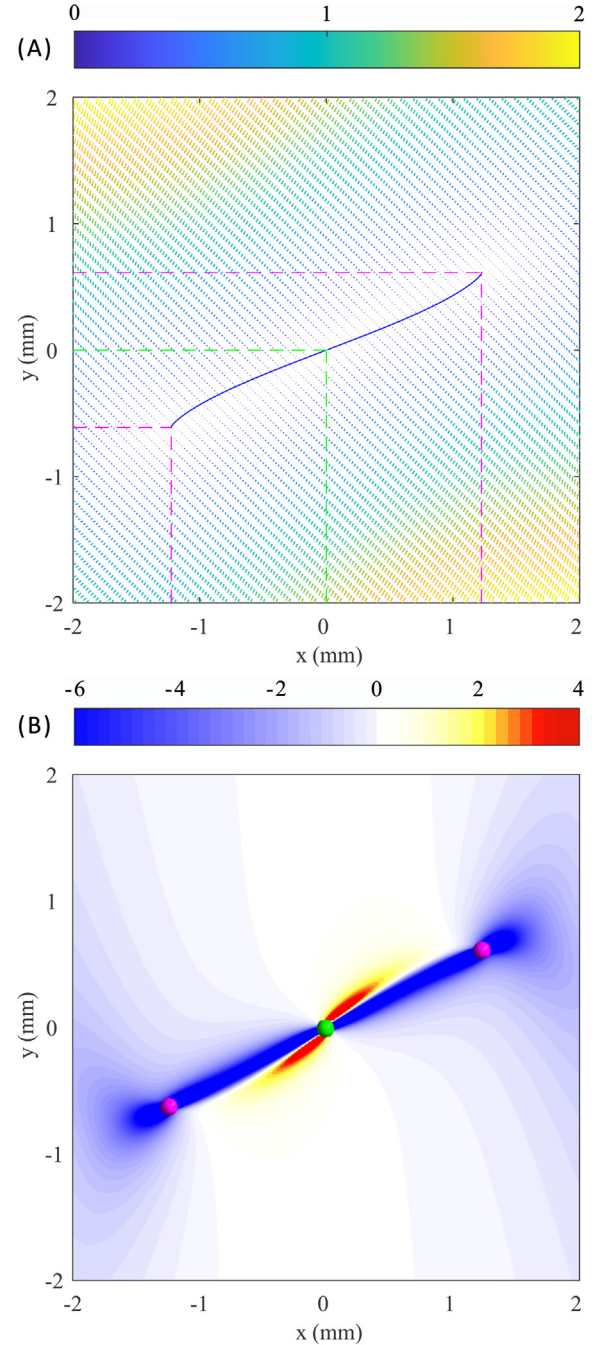

Fig. 6. (A) The two-dimensional vector field coloured by magnitude (every fifth vector point is visualised) with stable (attracting) manifold and critical point locations highlighted and (B) the divergence of the normalised vector field, which encloses the stable manifolds, with critical points also visualised (green and pink spheres). The results are in good agreement with the benchmarking proposed in the literature, validating the developed post-processing for the linear triangular surface mesh.

Topological shear variation index and critical point residence time: As the transient nature of blood flow could lead to variability in topological metrics, we also quantify the variation in WSS divergence over the cardiac cycle using the topological shear variation index (TSVI) [35,36], described by

$$TSVI = \left[\frac{1}{T}\int_0^T \left(\nabla\cdot\boldsymbol{\tau} - \overline{\nabla\cdot\boldsymbol{\tau}}\right)^2 dt\right]^{0.5}. \tag{12}$$
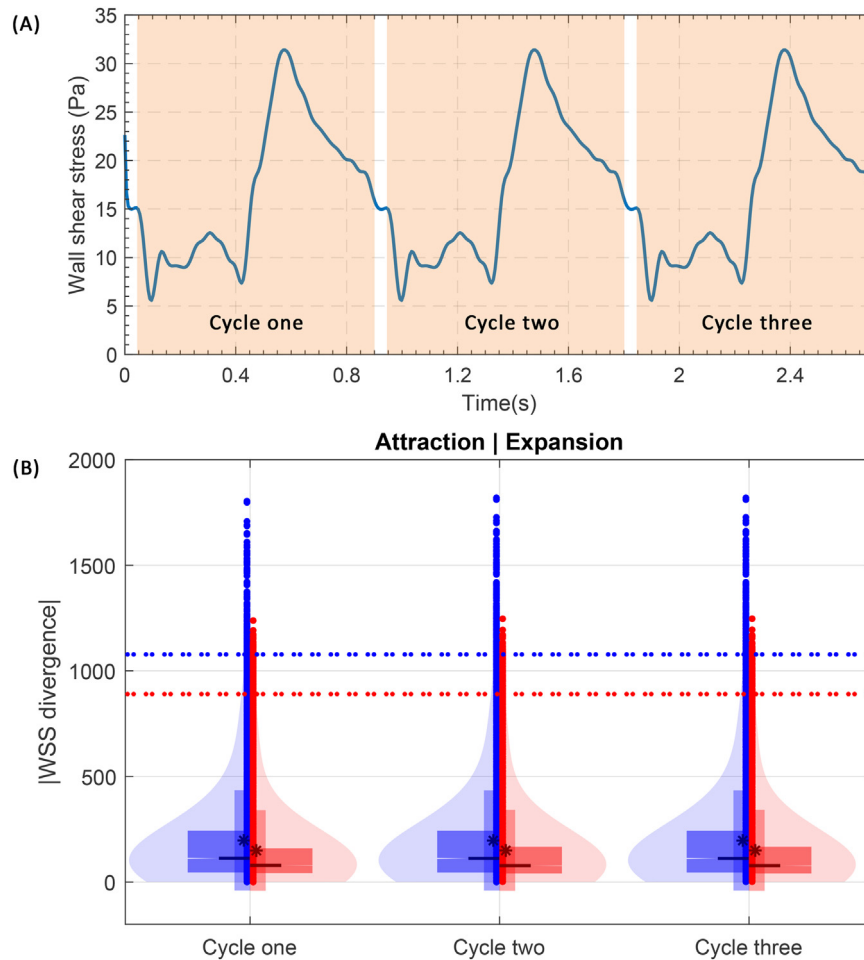
Fig. 7. Validation of convergence over three cardiac cycles. (A) Maximum WSS over the stenosis with the steps used for comparison of WSS divergence (steps 11–150) in each cardiac cycle highlighted in orange. (B) Violin plots of WSS divergence attraction and expansion regions for each cardiac cycle. Horizontal lines highlight the 99th percentiles which show less than one percent variation between the three cycles demonstrating sufficient convergence.

To further quantify how critical points move over the cardiac cycle their general residence time was calculated as the time each critical point, x, remains within an element face [30,33]

$$\mathrm{CP}_x(\eta) = \frac{\bar{A}(t)}{A_\eta(t)} \frac{1}{T} \int_0^T f(x,t), \tag{13}$$

where

$$f(x,t) = \begin{Bmatrix} 1 \Rightarrow x(t) \in \eta \\ 0 \Rightarrow x(t) \notin \eta \end{Bmatrix}. \tag{14}$$

Again, noting the time-dependence of the surface mesh area characteristics due to the coupled simulations. Throughout the remainder of the manuscript, when we refer to critical point locations, we refer to their general residence time calculated over the cardiac cycle, unless otherwise stated. Finally, to determine the number of cardiac cycles required to fully converge, a 43% stenosis simulation was run over three cycles. The maximum transient WSS and time averaged normalised WSS divergence were compared by omitting the first 10 timesteps of each cardiac cycle. This is approximately the number of steps required to reach dynamic equilibrium. When removing the first 10 timesteps of each cardiac cycle, less than one percent variation was seen in both the peak WSS magnitude and in the topological divergence contraction/extension regions (Fig. 7). Hence, one cardiac cycle was deemed sufficient for convergence in this case, provided the first 10-time steps were omitted. All subsequent simulations were carried out over one cardiac cycle with steps 11–150 used for post-processing. All post-

processing was carried out in MATLAB (version 2022a, Mathworks, Natick, MA).

2.8. Patient-specific application

Ethics approval for biomechanical simulation was granted from the Central Adelaide Local Health Network (CALHN) Research Services (CALHN Reference Number 14179) after the patient was recruited into the ongoing colchicine for coronary plaque modification in acute coronary syndrome (COCOMO-ACS) randomized-controlled trial (ACTRN12618000809235; Royal Adelaide Hospital HREC reference number: HREC/17/RAH/366) [89]. The right coronary artery (RCA) of a 68-year-old Caucasian male patient who presented with an acute NSTEMI in the setting of hypertension, type 2 diabetes mellitus, obstructive sleep apnoea and a body mass index of 34 was chosen for analysis. The patient had no history of smoking and no statin use in the four weeks preceding the index admission where invasive coronary angiography (ICA) and optical coherence tomography (OCT) imaging was performed before follow-up 18 months after the index admission, as per study design [89]. Lipid profiling at the index admission identified a total cholesterol of 3.1 mmol/L (low-density lipoprotein: 1.8 mmol/L, high-density lipoprotein: 0.6 mmol/L), triglycerides of 1.6 mmol/L and high-sensitivity C-reactive protein level of 23 mg/L. Results were then analysed in the context of lesion progression to demonstrate their potential to impact clinical understanding of a patients complex biomechanical stress state.
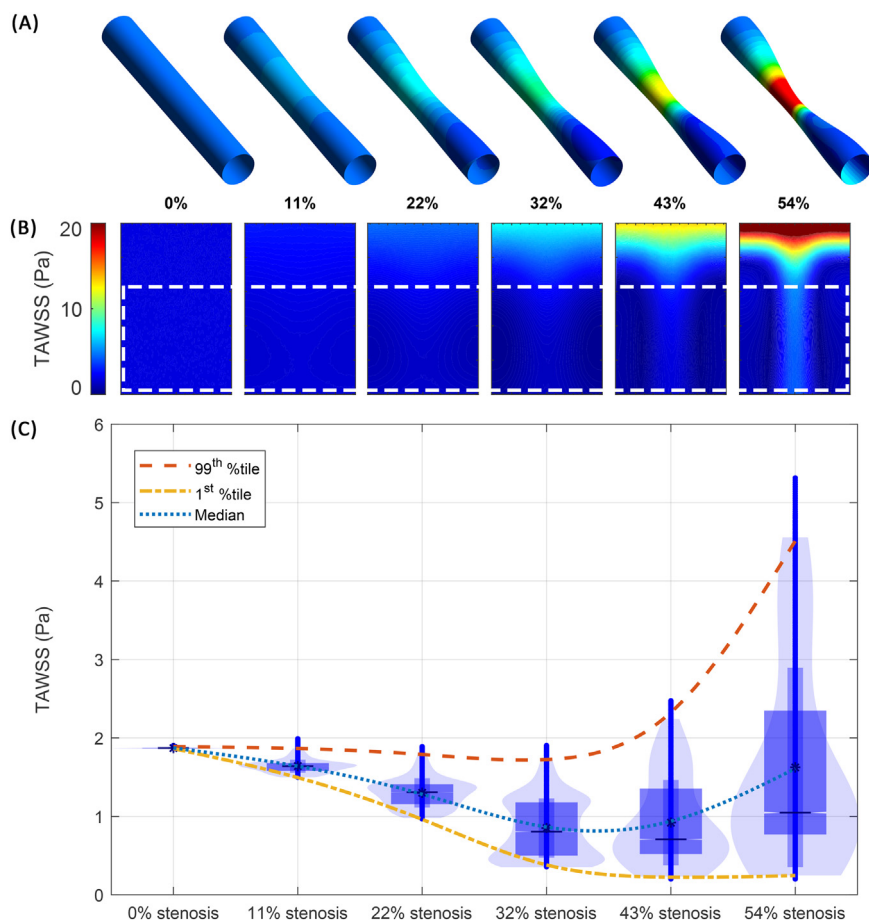
Fig. 8. (A) TAWSS contours on the wall region of interest for varying stenosis levels. (B) Unwrapped surface contours to visualise the TAWSS contour downstream of the maximum stenosis location. The region highlighted by the dotted white box is the region used to quantitively compare TAWSS values, visualised using violin plots in (C). Note the distinct separation of TAWSS kernel densities at 32% stenosis, suggesting a shift to more complex flow patterns. TAWSS – Time-averaged wall shear stress.

2.9. Patient-specific simulation setup

The patient specific simulation setup made use of our previously published simulation methodology [90]. Briefly, two angiographic planes had the OCT guidewire manually annotated before rotation and projection to determine the three-dimensional intersection curve (i.e. the guidewire location in three-dimensional space). OCT cross sections were then expertly annotated to extract cross sections of the lumen, lipid regions and the outer wall, which were subsequently analysed at follow-up to determine changes in vessel remodelling (i.e. lumen area), lipid arc and FCT (Supplemental Data Fig. S1). The outer wall was estimated in regions of high signal attenuation (i.e. in the presence of lipid) by using visible regions of the outer elastic membrane to fit an ellipse as an outer wall guide. The cross sections were then reconstructed into a three-dimensional solid model using ANSYS Design-Modeller. For simplicity, the numerical setup remained unchanged from Section 2.5, with the one exception of the coronary dynamics. Patient-specific dynamics were extracted from ICA using an optical flow branch tracking method in MATLAB's computer vision toolbox as previously proposed [38]. The branch was used to determine the three-dimensional dynamics of the artery section which were applied as boundary conditions on the structural domain. As already discussed in Section 2.4, the study of just one dynamical profile from one patient case limits the generalisability of results and should be considered as a preliminary finding that may warrant more rigorous future investigations.

2.10. Statistical analyses

To analyse correlations between FSI and CFD simulation results, Pearson's r correlation coefficient was calculated after ensuring normal contour data distribution by rank based inverse normal transformation. Linear fits were proposed and evaluated with the coefficient of determination (R^2). Locally weighted, non-parametric logistic regression (LOESS) was carried out in the patient-case to visualise the relationship between each of the 12 metrics and vessel remodelling (i.e. change in lumen area), change in lipid arc and change in FCT. Welch's t-test was used to test the null hypothesis of no variance in mean values between negative/positive remodelling, increase/decrease in lipid arc and increase/decreased FCT. All metrics were evaluated at the 5% significance level.

3. Results

3.1. Stenosis severity and lesion length

TAWSS was compared with stenosis percentage in the region downstream of the maximum stenosis in each of the six idealised models (0–54% stenosis) which were unwrapped for direct comparison (Fig. 8). Violin plots of the TAWSS distribution highlight a divergence in the kernel densities at 32% stenosis, suggesting the likely transition to complex flow patterns from 22 to 32% stenosis. Notably the minimum TAWSS magnitude reaches an inflection point in this range, before reaching its minimum value at 43%
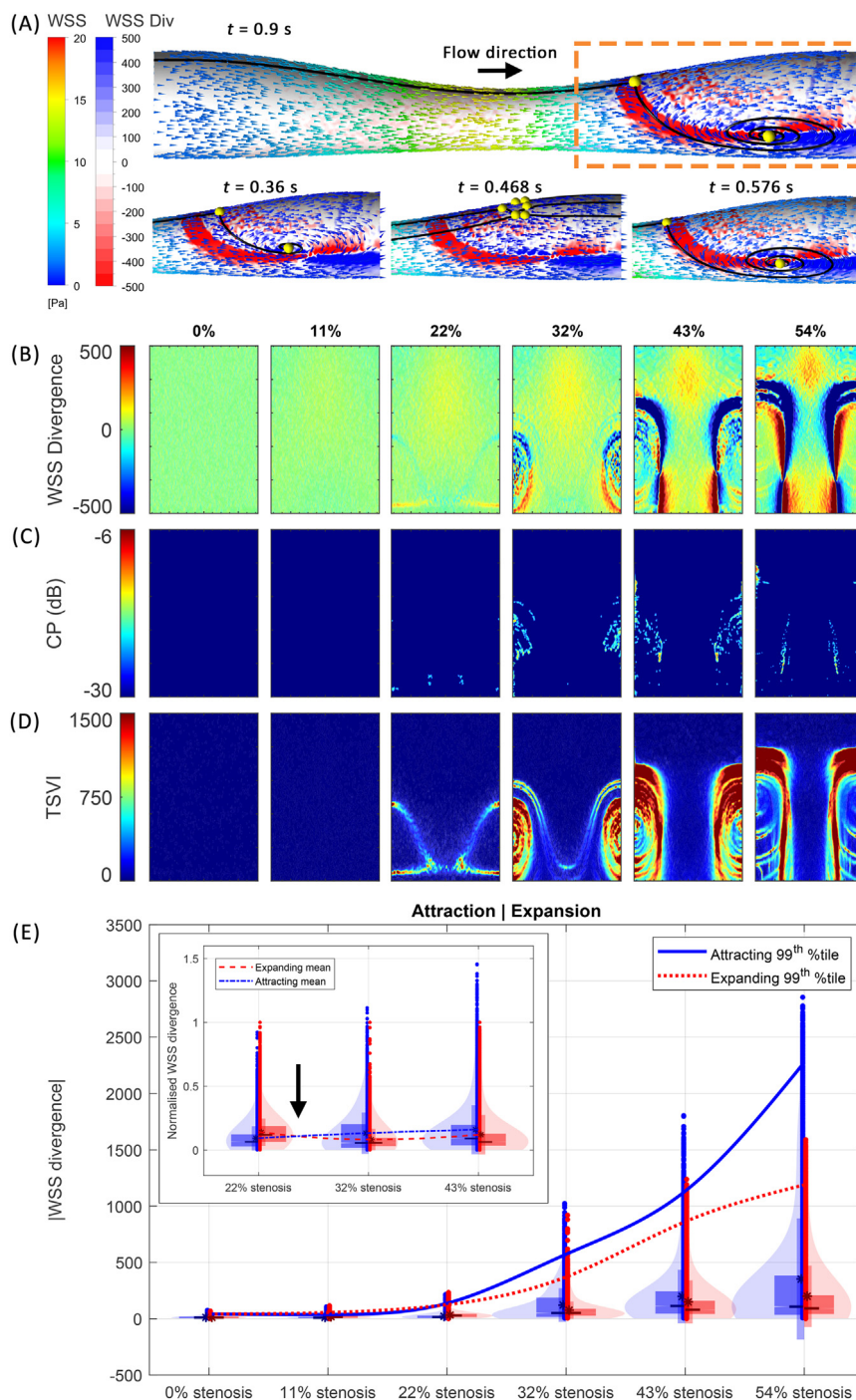
Fig. 9. (A) The instantaneous ($t = 0.9$ s) WSS vector field coloured by magnitude with streamlines (black lines) connecting CP locations (yellow spheres) overlaid with the time averaged WSS divergence contour. Inset, variations at peak systolic pressure ($t = 0.36$ s), peak diastolic velocity ($t = 0.576$ s) and the time corresponding to the secondary pressure pulse ($t = 0.468$ s). (B) WSS divergence contours downstream from varying stenosis levels. (C) CP location contours downstream from varying stenosis levels in logarithmic scale. (D) TSVI contours downstream from varying stenosis levels. (E) Violin plots of the relationship between attracting and expanding WSS regions across increasing stenosis levels. Inset, the relationship between 22%, 32% and 43% stenosis normalised against the maximum expanding value to highlight the crossover in attracting/expanding zone medians that occurs at 25% stenosis (black arrow). WSS –Wall shear stress. CP – Critical point. TSVI – Topological shear variation index.

stenosis while the peak TAWSS magnitude diverges from the minimum and exponentially increases beyond 32%.

Investigating in more detail, the divergence of the normalised WSS vector field, its associated critical points, and the TSVI were compared (Fig. 9). Black lines representing the manifolds connecting the critical points were visualised as yellow spheres (Fig. 9a). Notably, a significant variation over the cardiac cycle is seen, with the transition from systolic to diastolic period effectively annulling

the recirculation regions that are otherwise present, further highlighting the importance of accurately modelling the effects of transient pressure pulses that propagate throughout the coronary vasculature. This also highlights the important factor that a critical point will likely never be a critical point over the entire cardiac cycle, due to the significant changes in velocity/pressure profiles between cardiac phases. Unwrapping the WSS divergence, critical points and the TSVI downstream of the maximum stenosis

for comparison, the WSS divergence undergoes a visually significant change from 22 to 32% stenosis, with the critical points and TSVI further highlighting this (Fig. 9b–d). The TSVI showed a strong variability in the WSS divergence as early as 22% stenosis, highlighting a potentially significant effect on WSS topology when considering the transient nature of coronary blood flow. Violin plots of the contraction and expansion regions in the WSS divergence quantitatively showed 22% stenosis as a critical point beyond which WSS divergence was amplified. Shown inset, the median contraction force imbalances the expanding force at 25% stenosis, further suggesting this as a critical, flow altering stenosis range (Fig. 9e).

In agreement with WSS divergence, a visually appreciable change in multi-directionality was seen at either 22 or 32% stenosis (Fig. 10). Of note, a significant difference was seen between TrWSS, WSSax and WSSsec and their normalised versions, the CFI, WSŜaxe and WSŜsec, respectively. This highlighted that multi-directional WSS metrics were heavily influenced by WSS magnitude, suggesting that their normalised versions could be a more meaningful metric for studying disease progression that is also independent of WSS magnitude alone. The impact of lesion length at a constant 43% stenosis is shown in Fig. 11. The unwrapped contours downstream of the maximum stenosis (Fig. 11b–d) show changes following the shortening stenosis. Critical point locations show a reduction in motion over the cardiac cycle as the lesion length decreases, leading to an increased residence time. Similarly, the TSVI appears to concentrate more closely at the lesion shoulder with a longer, but less significant magnitude, variable flow region downstream of the maximum stenosis. This suggests a more rapid fluctuation in the WSS divergence over the cardiac cycle as the lesion length decreases. Quantifying the WSS divergence contraction and expansion regions highlighted the exponentially increasing strength of the contraction region that diverges from the stagnant expansion region magnitude (Fig. 11E).

The remaining eight multi-directional WSS showed similar patterns, whereby the metrics follow the shortening lesion closely, amplifying each multi-directional measures magnitude (Fig. 12). The TrWSS showed the most significant change in the region immediately downstream of the stenosis which contributed to the reducing RRT at the same location. To better quantify how lesion length and stenosis percentage impacted multi-directional/topological WSS measures, the 90th percentiles and mean of each metric were assessed, with comparisons made to the minimum, maximum and mean TAWSS magnitudes previously discussed (Fig. 13). For the RRT, TSVI and CFI, a 22% stenosis presented the first significant changes, while 32% appeared more significant for the OSI and TrWSS. The WSSsec and expanding WSS divergence components tracked more closely with maximum downstream WSS magnitude and increased most significantly beyond 43% stenosis. Interestingly, 90th percentile values for CFI, OSI, RRT and TrWSS all decreased beyond 43% stenosis, while the mean CFI and TSVI stabilised in this range. With shortening lesion length, CFI, TrWSS, OSI, RRT and TSVI all show a decreasing trend while the remaining metrics all increased. This quantitatively highlights the nonlinearity of the relationship between lesion morphology and multi-directional/topological WSS metrics.

3.2. FSI vs CFD

Detail on the transient magnitude at three different locations over the lumen surface can be found in Supplemental Data Fig. S2, where the difference in peak WSS magnitude between CFD and FSI simulations mirrored that of previous investigations [40,41]. However, the downstream region saw exponentially increasing differences in WSS magnitude not previously discussed. Furthermore, the impact of the backward propagating pressure pulse captured

using higher order transient velocity and pressure waves resulted in significant variability in the transition between systolic to diastolic phases which could exacerbate differences in WSS multi-directionality/topology.

Detailed comparisons of the intraclass correlation between TAWSS and each of the remaining 11 metrics within each simulation (CFD and FSI simulations with varying dynamic boundary conditions) are made in Table 4. Interestingly, TrWSS and the CFI showed a stronger correlation with TAWSS than other multi-directional WSS metrics. Throughout each simulation, WSSsec and its normalised version, WSŜsec, consistently showed no significant correlation with TAWSS, as well as an r value suggestive of a nonlinear (or no) relationship. While the WSS divergence had a significant relationship, its r value also consistently suggested that its relationship with TAWSS was weak or nonlinear. The interclass correlation between CFD and FSI simulations were calculated to analyse respective changes in the relationship brought about by differing boundary conditions (Table 5). Complete intra- and interclass correlations are presented in Supplemental Data Tables S1–6. These results highlight that most results showed strong correlations between CFD and FSI simulations despite dynamic boundary condition changes. TrWSS, CFI, WSSsec, WSŜsec and WSS divergence were the exceptions, with greater than 10% change in r values in 43% stenosis models.

We therefore investigated their relationships in more detail. Comparisons between all 12 WSS metrics in FSI and CFD simulations at 22 and 43% stenosis, as well as at 43% stenosis with a 10 mm lesion length, are shown in Fig. 14 and 15. The strong linear relationship between TAWSS in CFD and FSI simulations confirms previous results showing the systematic reduction in TAWSS due to the compliant artery wall. The impact of coronary dynamics was only marginally visible in the 43% stenosis simulation (18 mm lesion length), producing a further reduction in TAWSS magnitude across the lumen wall. Multi-directional metrics saw a much more significant change. TrWSS and CFI showed significant variability with both added dynamics and dynamic direction, with the inclusion of lumen wall geometrical properties (i.e. using the surface normal in their calculation) producing significant variability due to the compliance introduced in FSI simulations. Similarly, the correlations shown in Fig. 15 highlighted that the relationship between CFD and FSI simulations are not straightforward, while the addition of dynamics further modifies this relationship. The TSVI was suppressed by 94% at 22% stenosis, while no significant variation appeared at a more significant 43% stenosis (Fig. 16). Unwrapped contours of each of the topological WSS metrics in all FSI simulations can be found in Supplemental Data Figs. S3 and S4 for further visualisation.

3.3. Patient-specific case

TAWSS differences between the dynamic FSI and CFD simulations highlighted that TAWSS is reduced in the FSI simulation predominantly in the cross-sectional regions that undergo moderate to high TAWSS in the CFD simulation (Supplemental Data Fig. S5). The scatter plot further shows differences between the simulations, with a linear correlation that is weaker than any of the idealised simulations presented in Section 3, albeit a relationship that is still significant. The intraclass correlation coefficients between TAWSS and each topological WSS metric in the three simulations are presented in Table 6. TrWSS, CFI, WSSsec, WSŜsec and WSS divergence showed a weak linear relationship suggesting either nonlinearity or other influences impacting the relationship with TAWSS. Interestingly, the interclass correlation coefficients (Table 7) all show strongly linear and significant ($p < 0.001$) relationships between both FSI simulations and CFD. Complete intra-
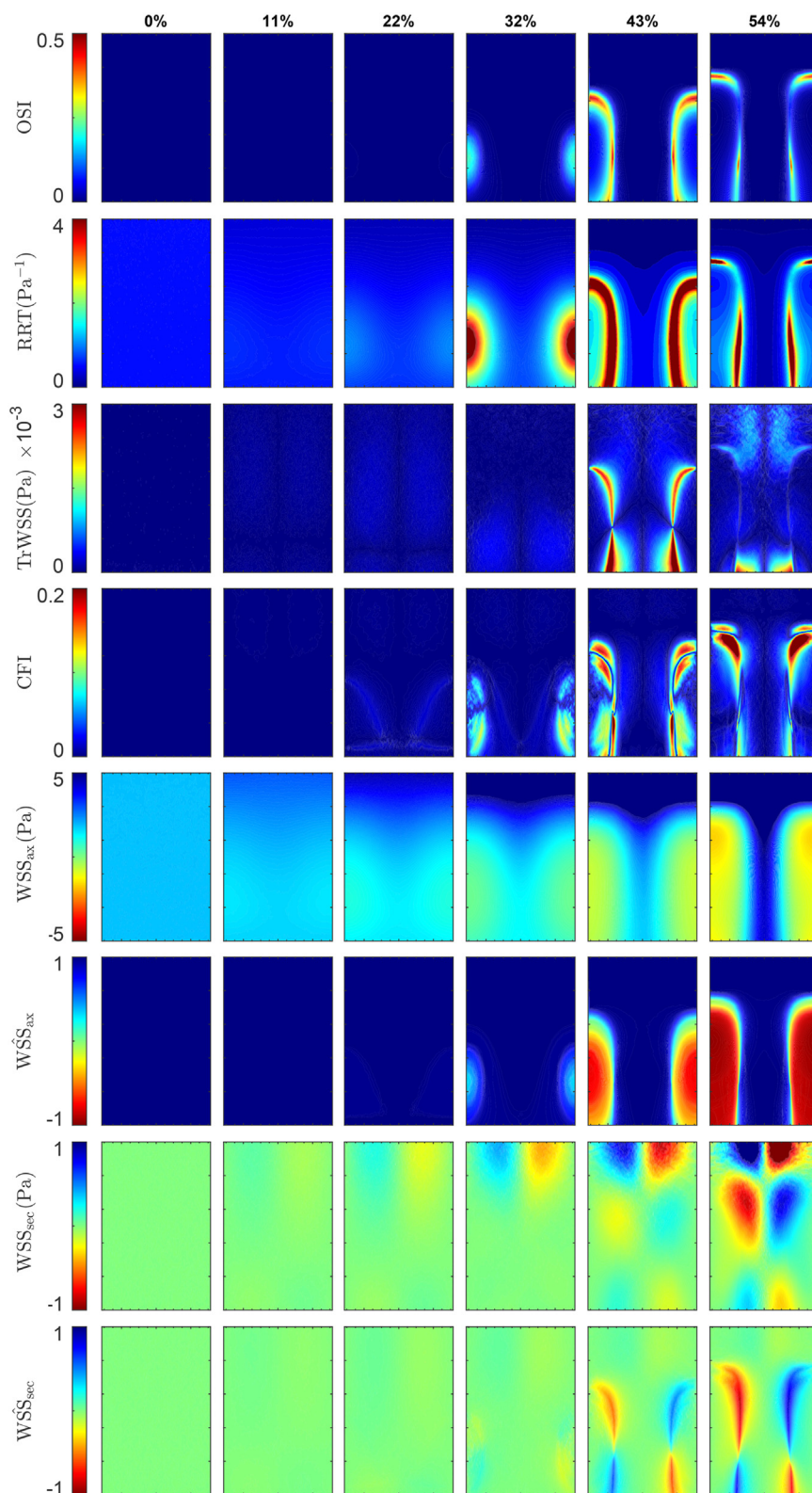
Fig. 10. Unwrapped contours of varying stenosis levels downstream of the maximum stenosis location for: OSI – Oscillatory shear index; RRT – Relative residence time; Tr WSS – Transverse wall shear stress; CFI – Cross flow index; WSSax – Axial wall shear stress; WSŜaxe – Normalised axial wall shear stress; WSSsec – Secondary wall shear stress; WSŜsec – Normalised secondary wall shear stress.

Table 4

Intraclass correlation coefficients (r; p-value) between TAWSS and WSS metrics within CFD and FSI simulations, but with varying dynamic boundary conditions imposed on the FSI simulations. Bold values highlight relationships that are *not* significant ($p>0.05$). Highlighted cells show relationships that have a weak correlation coefficient ($-0.5<r<0.5$), suggesting outside influences or nonlinearity of the relationship. Complete intraclass correlation coefficients for 22% and 43% stenosis simulations are available in Supplemental Data, Table S1-3. CFD – Computational fluid dynamics; CFI – Cross flow index; CP – Critical point residence time; D – Dynamic; Div – Wall shear stress Divergence; FSI – Fluid-structure interaction; ID – Inverse dynamics; OSI – Oscillatory shear index; RRT – Relative residence time; S – Static (no motion); TAWSS – Time averaged wall shear stress; TrWSS – Transverse wall shear stress; TSVI – Topological shear variation index; WSSax – Axial wall shear stress; WSŜaxe – Normalised axial wall shear stress; WSŜsec – Normalised secondary wall shear stress; WSSsec – Secondary wall shear stress.

|			OSI	RRT	TrWSS	CFI	WSSax	WSŜaxe	WSSsec	WSŜsec	Div	TSVI	CP
TAWSS	22% stenosis 18 mm lesion	CFD	−0.71; $p<0.001$	−1.0; $p<0.001$	−0.14; $p<0.001$	−0.39; $p<0.001$	1.0; $p<0.001$	0.75; $p<0.001$	−0.00010; $p=0.98$	−0.0011; $p=0.77$	0.044; $p<0.001$	−0.75; $p<0.001$	−0.0032; $p=0.39$
		FSI-S	−0.83; $p<0.001$	−1.0; $p<0.001$	−0.45; $p<0.001$	−0.56; $p<0.001$	1.0; $p<0.001$	0.91; $p<0.001$	0.00089; $p=0.81$	−0.00046; $p=0.9$	0.10; $p<0.001$	−0.74; $p<0.001$	−0.018; $p<0.001$
		FSI-D	−0.66; $p<0.001$	−1.0; $p<0.001$	−0.51; $p<0.001$	−0.38; $p<0.001$	1.0; $p<0.001$	0.44; $p<0.001$	0.0011; $p=0.76$	0.00025; $p=0.95$	0.062; $p<0.001$	−0.78; $p<0.001$	−0.019; $p<0.001$
		FSI-ID	−0.70; $p<0.001$	−1.0; $p<0.001$	−0.52; $p<0.001$	−0.51; $p<0.001$	1.0; $p<0.001$	0.43; $p<0.001$	0.00089; $p=0.81$	−0.0010; $p=0.78$	0.063; $p<0.001$	−0.84; $p<0.001$	−0.016; $p<0.001$
	43% stenosis 18 mm lesion	CFD	−0.86; $p<0.001$	−0.98; $p<0.001$	−0.48; $p<0.001$	−0.73; $p<0.001$	0.85; $p<0.001$	0.76; $p<0.001$	0.0012; $p=0.75$	−0.00070; $p=0.85$	0.22; $p<0.001$	−0.85; $p<0.001$	−0.20; $p<0.001$
		FSI-S	−0.90; $p<0.001$	−0.97; $p<0.001$	−0.58; $p<0.001$	−0.76; $p<0.001$	0.85; $p<0.001$	0.81; $p<0.001$	0.00086; $p=0.81$	0.0046; $p=0.21$	0.13; $p<0.001$	−0.82; $p<0.001$	−0.21; $p<0.001$
		FSI-D	−0.89; $p<0.001$	−0.97; $p<0.001$	−0.57; $p<0.001$	−0.75; $p<0.001$	0.85; $p<0.001$	0.81; $p<0.001$	0.0061; $p=0.098$	−0.00063; $p=0.86$	0.27; $p<0.001$	−0.82; $p<0.001$	−0.20; $p<0.001$
		FSI-ID	−0.89; $p<0.001$	−0.97; $p<0.001$	−0.61; $p<0.001$	−0.76; $p<0.001$	0.86; $p<0.001$	0.82; $p<0.001$	0.0035; $p=0.34$	0.0031; $p=0.39$	0.28; $p<0.001$	−0.83; $p<0.001$	−0.19; $p<0.001$
	43% stenosis 10 mm lesion	CFD	−0.86; $p<0.001$	−0.98; $p<0.001$	−0.14; $p<0.001$	−0.65; $p<0.001$	0.71; $p<0.001$	0.67; $p<0.001$	−0.0015; $p=0.67$	−0.0016; $p=0.65$	0.17; $p<0.001$	−0.77; $p<0.001$	−0.14; $p<0.001$
		FSI-S	−0.81; $p<0.001$	−0.97; $p<0.001$	−0.15; $p<0.001$	−0.60; $p<0.001$	0.73; $p<0.001$	0.71; $p<0.001$	−0.00049; $p=0.89$	0.0012; $p=0.75$	0.27; $p<0.001$	−0.73; $p<0.001$	−0.18; $p<0.001$
		FSI-D	−0.83; $p<0.001$	−0.98; $p<0.001$	−0.13; $p<0.001$	−0.59; $p<0.001$	0.72; $p<0.001$	0.70; $p<0.001$	−0.00022; $p=0.95$	0.0011; $p=0.76$	0.30; $p<0.001$	−0.75; $p<0.001$	−0.18; $p<0.001$
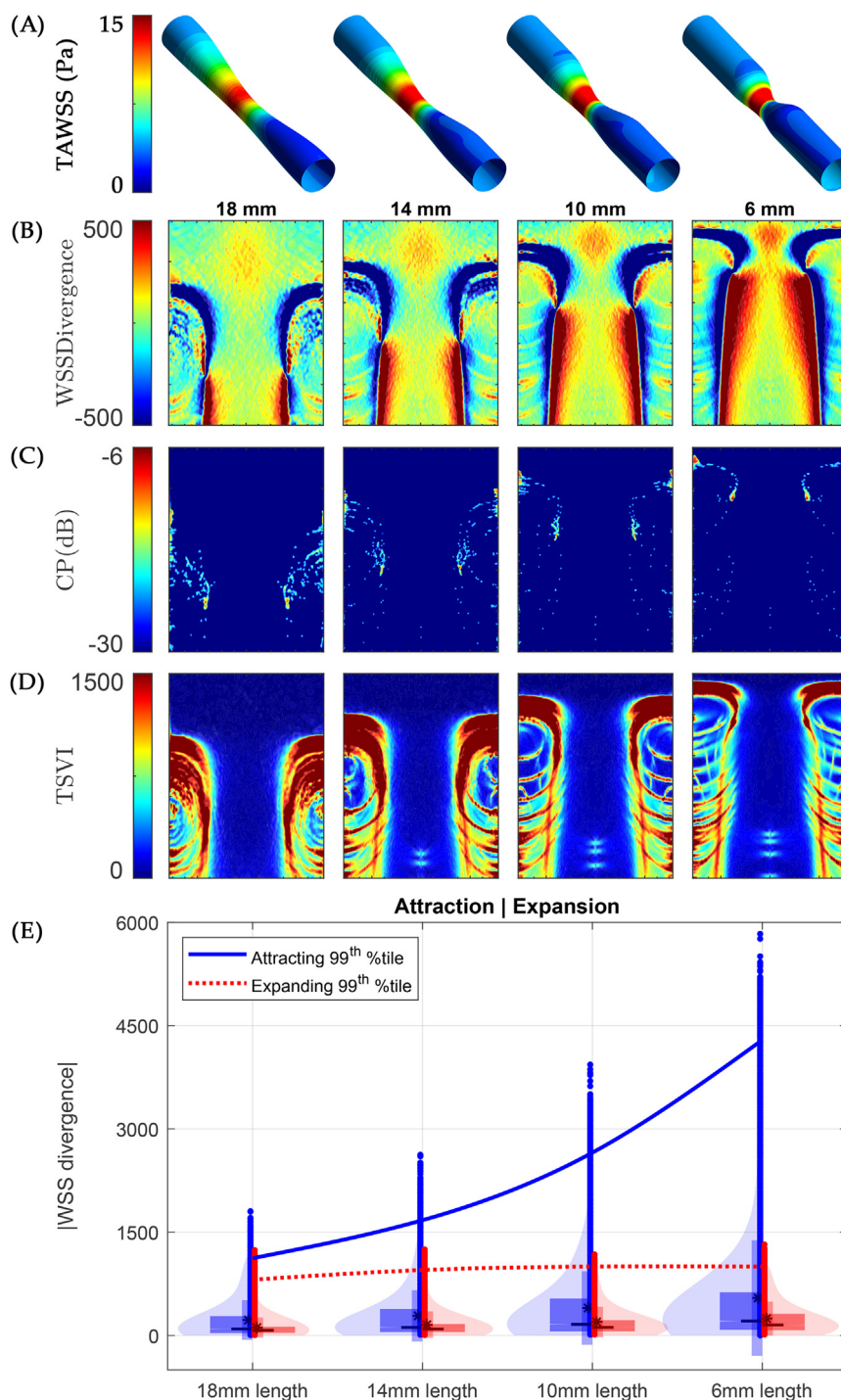
Fig. 11. TAWSS and associated normalised WSS vector field divergence results at 43% stenosis with decreasing lesion length. (A) TAWSS contours on the idealised geometries. (B) Unwrapped contours of the normalised WSS vector field divergence downstream of the maximum stenosis. (C) Unwrapped contours of the critical point (CP) residence time potted with logarithmic scale. (D) TSVI highlighting the variation in the WSS divergence over the cardiac cycle. (E) Violin plots of the attracting and expanding regions of the WSS divergence highlighting the divergence between the two regions as lesion length decreases.

and interclass correlation coefficients are available in the Supplemental Data Tables S7 and S8.

The exceptions were OSI and TrWSS, whose relationships are presented in more detail in Supplemental Data Figs. S6 and S7. Of note, the variation in TrWSS between CFD and the static and dynamic FSI analyses was the most significant variation seen. These changes are attributable to the use of the lumen wall normal vector in the calculation of TrWSS and CFI, a factor which is significantly impacted by the wall compliance and motion in FSI. Extend-

ing these comparisons, the relationships between axial and secondary WSS measures are shown in Supplemental Data Figs. S8 and S9. In both cases, the normalised versions (i.e. independent of WSS magnitude) showed variation with the addition of coronary dynamics. The WSŜsec saw a 700% decrease in magnitude compared to CFD in the more proximal region, however, their R^2 coefficients remained similar, suggesting that dynamics homogeneously altered their multi-directionality. The WSS divergence and its transient metric, the TSVI, are also presented in Supplemental
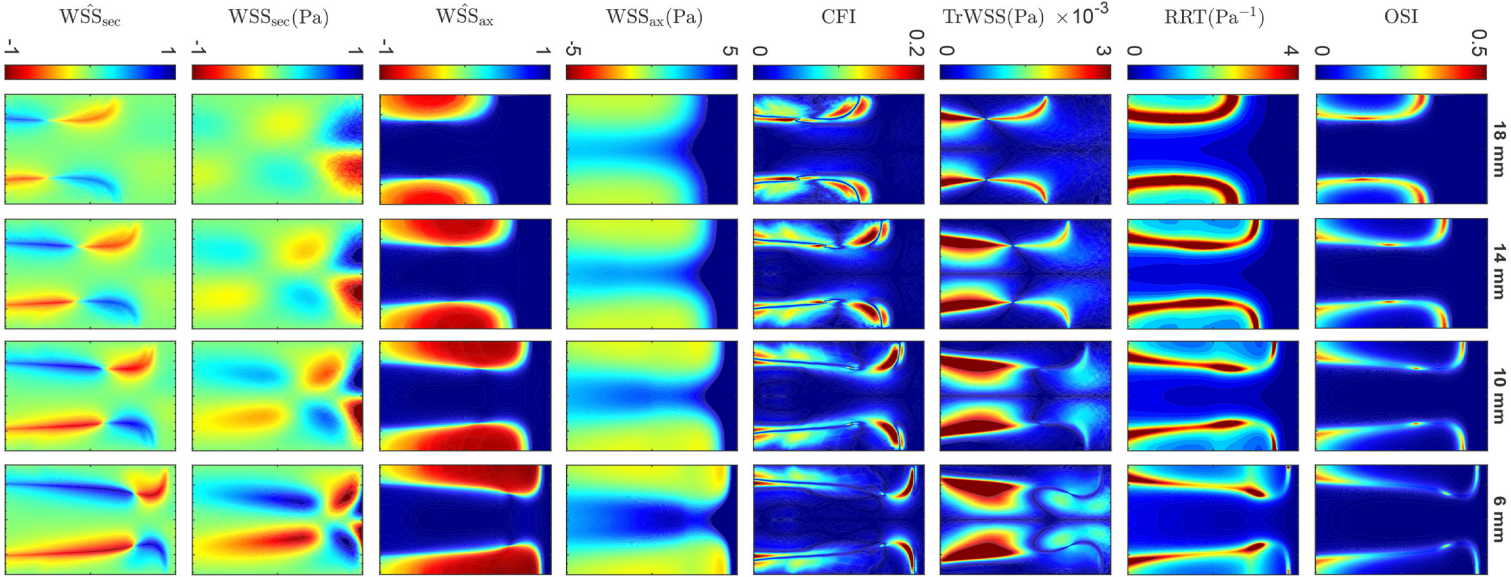
Fig. 12. Unwrapped contours of multi-directional wall shear stress measures with varying lesion length (18–6 mm) at a constant 43% stenosis. OSI – Oscillatory shear index; RRT – Relative residence time; Tr WSS – Transverse wall shear stress; CFI – Cross flow index; WSSax – Axial wall shear stress; WSŜax – Normalised axial wall shear stress; WSSsec – Secondary wall shear stress; WSŜsec – Normalised secondary wall shear stress.

Table 5

Interclass correlation coefficients (r; p-value) between WSS derived metrics in CFD and FSI simulations, but with varying dynamic boundary conditions imposed on the FSI simulations. Coefficients are compared at 0%, 22% and 43% stenosis as well as 18 mm and 10 mm lesion length. Bold values show significant (>10%) change in correlation coefficient with varied boundary conditions. Complete interclass correlation coefficients for 22% and 43% stenosis simulations are available in Supplemental Data, Table S4-6. S – Static (no motion); D – Dynamic; ID – Inverse dynamics; Other abbreviations as in Table 4.

|		WSS derived metric (CFD)											
		TAWSS	OSI	RRT	TrWSS	CFI	WSSax	WSŜaxe	WSSsec	*WSŜsec*	Div	TSVI	CP
FSI (stenosis; lesion length; boundary condition)	22%; 18 mm; S	0.93; $p<0.001$	0.90; $p<0.001$	0.93; $p<0.001$	0.90; $p<0.001$	0.73; $p<0.001$	0.93; $p<0.001$	0.85; $p<0.001$	0.93; $p<0.001$	0.74; $p<0.001$	0.56; $p<0.001$	0.67; $p<0.001$	−6.8e-05; $p = 0.99$
	22%; 18 mm; D	0.94; $p<0.001$	0.84; $p<0.001$	0.94; $p<0.001$	0.86; $p<0.001$	0.73; $p<0.001$	0.94; $p<0.001$	0.58; $p<0.001$	0.93; $p<0.001$	0.77; $p<0.001$	0.58; $p<0.001$	0.70; $p<0.001$	−4.5e-05; $p = 0.99$
	22%; 18 mm; ID	0.94; $p<0.001$	0.85; $p<0.001$	0.94; $p<0.001$	0.84; $p<0.001$	0.73; $p<0.001$	0.94; $p<0.001$	0.46; $p<0.001$	0.91; $p<0.001$	0.80; $p<0.001$	0.58; $p<0.001$	0.73; $p<0.001$	−3.0e-05; $p = 0.99$
	43%; 18 mm; S	0.95; $p<0.001$	0.91; $p<0.001$	0.95; $p<0.001$	0.55; $p<0.001$	0.69; $p<0.001$	0.99; $p<0.001$	0.93; $p<0.001$	0.63; $p<0.001$	0.36; $p<0.001$	0.36; $p<0.001$	0.86; $p<0.001$	0.11; $p<0.001$
	43%; 18 mm; D	0.95; $p<0.001$	0.95; $p<0.001$	0.96; $p<0.001$	0.63; $p<0.001$	0.78; $p<0.001$	0.99; $p<0.001$	0.93; $p<0.001$	0.71; $p<0.001$	0.59; $p<0.001$	0.56; $p<0.001$	0.89; $p<0.001$	0.089; $p<0.001$
	43%; 18 mm; ID	0.95; $p<0.001$	0.95; $p<0.001$	0.96; $p<0.001$	0.65; $p<0.001$	0.79; $p<0.001$	0.99; $p<0.001$	0.94; $p<0.001$	0.71; $p<0.001$	0.60; $p<0.001$	0.60; $p<0.001$	0.91; $p<0.001$	0.093; $p<0.001$
	43%; 10 mm; S	0.94; $p<0.001$	0.94; $p<0.001$	0.93; $p<0.001$	0.76; $p<0.001$	0.76; $p<0.001$	0.99; $p<0.001$	0.96; $p<0.001$	0.87; $p<0.001$	0.96; $p<0.001$	0.73; $p<0.001$	0.89; $p<0.001$	0.16; $p<0.001$
	43%; 10 mm; D	0.94; $p<0.001$	0.94; $p<0.001$	0.93; $p<0.001$	0.78; $p<0.001$	0.78; $p<0.001$	0.99; $p<0.001$	0.97; $p<0.001$	0.86; $p<0.001$	0.95; $p<0.001$	0.74; $p<0.001$	0.90; $p<0.001$	0.16; $p<0.001$
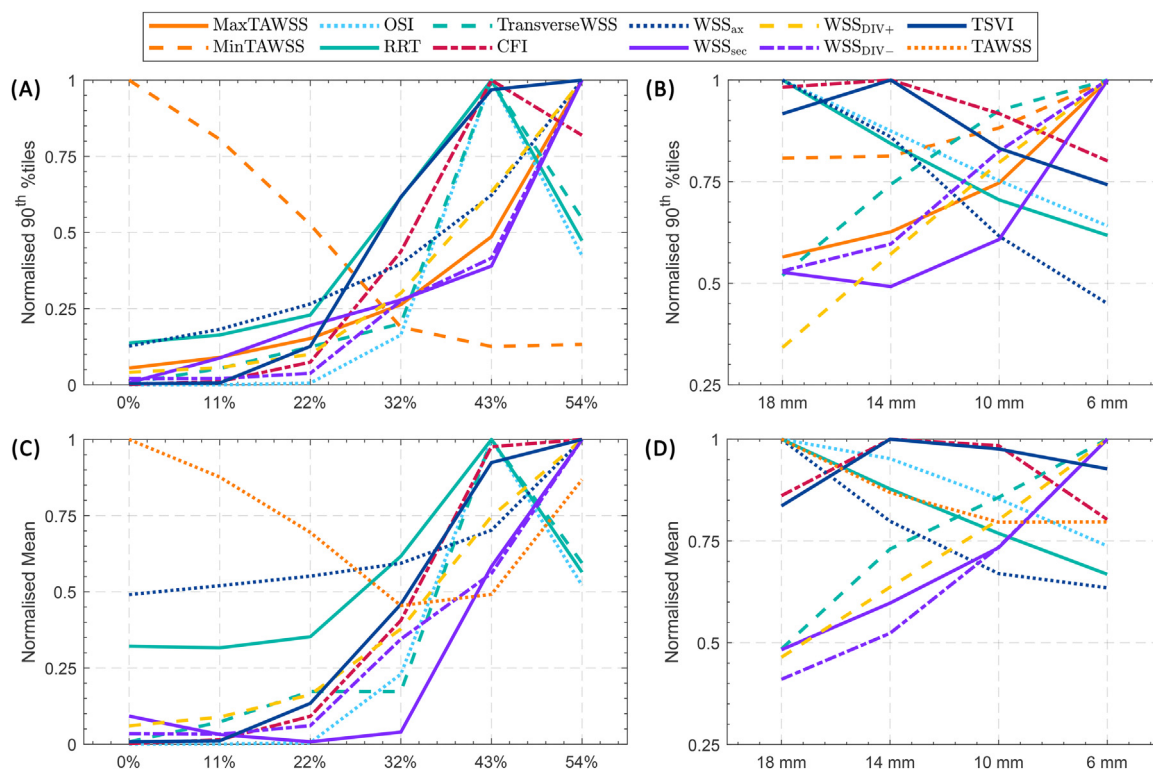
Fig. 13. Comparison of the 90th percentiles (A, B) and mean values (C, D) downstream of the stenosis. Values are normalised against each metrics maximum value to highlight their relationship with stenosis severity (A, C) and lesion length (B, D).

Data Fig. S10. Subtle differences can be seen in the unwrapped WSS divergence contours, particularly in the more proximal region that undergoes the first expansion in lumen area (in the same region of altered WSŜsec). This region sees both a significant increase and decrease in WSS divergence magnitude that results in significant TSVI variability. Both the WSS divergence and TSVI present a weakly linear relationship between FSI and CFD simulations, with variability in the linear slope with the added dynamic boundary condition.

To determine if these variations were significant enough to alter the ability to associate WSS results with vasculature changes a two-fold approach was undertaken. Results from these associations with the measured change in lumen area (i.e. identifying vessel remodelling) is highlighted in Fig. 17. Associations with changes in lipid plaque morphology are presented in Supplemental Data Figs. S11 and S12. Here the outer ring describes the LOESS fits while the inner ring shows the associated *t*-test, with a larger value suggesting a stronger variation between means, and R^2 results to visualise the strength of each metrics association with vasculature changes and how they vary between the three simulations. The strength of the association between TAWSS and negative (red arrows) and positive (green arrows) remodelling was decreased in FSI simulation due to the areas of high WSS being reduced due to the compliance of the wall. The rings in the inner plot showcased the TAWSS *t*-test result for comparison with the remaining eleven metrics. Of note, TrWSS and CFI showed the strongest associations with vessel remodelling in CFD simulations. However, these associations were significantly damped in both static and dynamic FSI, where OSI and WSŜax showed the strongest associations. Interestingly, the normalised components of WSSax and WSSsec (black arrows) both showed stronger associations with remodelling that their counterparts which included WSS magnitude (purple arrows). Furthermore, the TSVI showed an association with vessel remodelling that was equally as strong as TAWSS, highlighting the im-

portance of the transient nature of flow in modulating changes in the vasculature.

Unlike vessel remodelling, there appears no significant change in the strength of associations between TAWSS in CFD and FSI simulations for lipid arc changes (Supplemental Data Fig. S11). Like vessel remodelling, TrWSS and CFI showed stronger associations between increasing and decreasing lipid arc, while the normalised axial and secondary WSS components showed stronger differentiation in the dynamic FSI simulation. Fibrous cap thickness changes were most strongly associated with OSI and normalised axial WSS in CFD simulations (Supplemental Data Fig. S12). This held true in both FSI simulations, with the addition of secondary WSS and RRT providing similar associations. TSVI also presented an association as strong as TAWSS, although both FSI simulations resulted in a significant reduction in the differences in means between thinning and thickening fibrous cap locations. The R^2 coefficient for all metrics varied significantly between CFD, static FSI and dynamic FSI, highlighting how wall compliance and coronary dynamics could impact associations between WSS metrics and vasculature changes.

4. Discussion

These results show that the influence of coronary dynamics appears most substantial in lesions with less 'significant' morphological variability. In other words, lesions with more severe stenosis or changes in the geometry appear to be less impacted by coronary dynamics while in the presence of strong geometric nonlinearities, simulations with and without coronary dynamics produce comparable WSS topological results. In less severe artery stenoses these multi-directional/topological results vary more significantly. This could have important implications for assessing the early stages of atherosclerosis development (or non-culprit lesions) before significant, flow limiting stenosis is reached, a point previously highlighted in Section 2.2. This also brings up an intriguing consider-
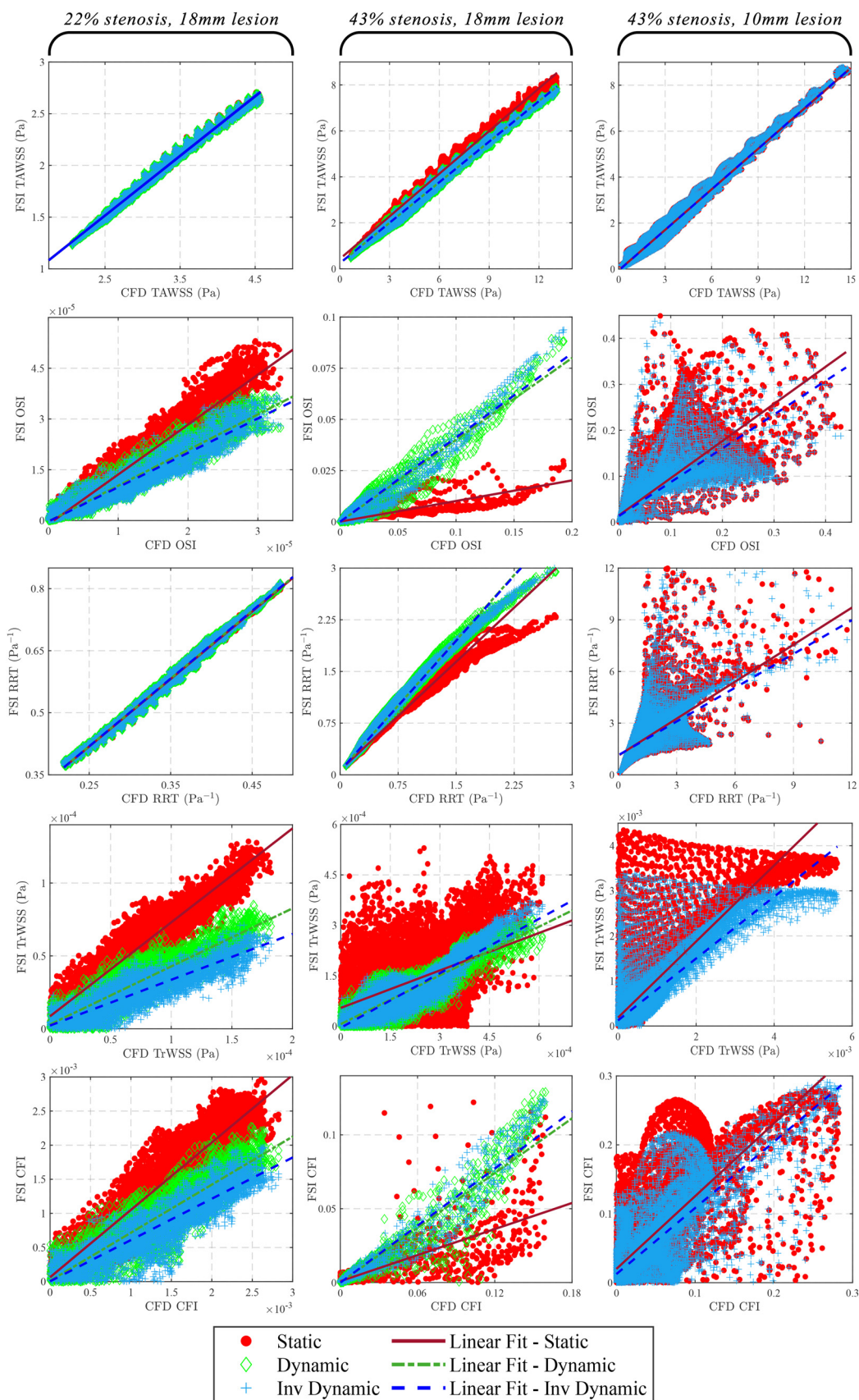
Fig. 14. Comparison of TAWSS, OSI, RRT, TrWSS and CFI contour data at 22% stenosis (18 mm lesion length), 43% stenosis (18 mm lesion length) and 43% stenosis (10 mm lesion length) shown by each of the three columns, respectively. The impact of different simulations (FSI vs CFD) and boundary conditions can be seen in TrWSS and CFI which both make use of the wall geometrical properties in their calculation. CFD – Computational fluid dynamics; CFI – Cross flow index; FSI – Fluid-structure interaction; OSI – Oscillatory shear index; RRT – Relative residence time; TAWSS – Time averaged wall shear stress; Tr WSS – Transverse wall shear stress.
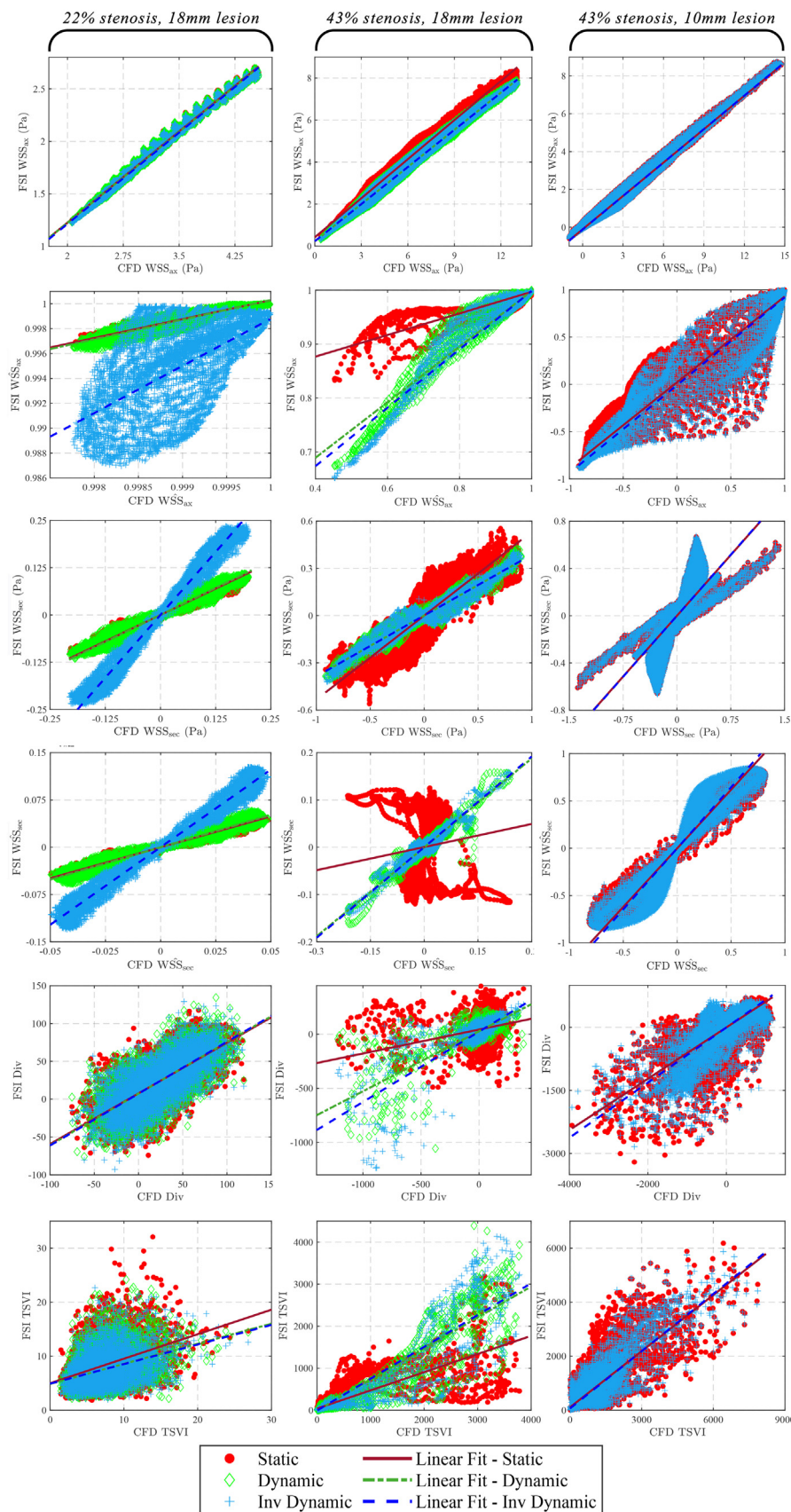
Fig. 15. Comparison of WSSax, WSŜaxe, WSSsec, WSŜsec, WSS divergence and TSVI contour data between CFD and FSI simulations with varying boundary conditions at 22% stenosis (18 mm lesion length), 43% stenosis (18 mm lesion length) and 43% stenosis (10 mm lesion length) shown by each of the three columns, respectively. CFD – Computational fluid dynamics; FSI – Fluid-structure interaction; WSSax – Axial wall shear stress; WSŜaxe – Normalised axial wall shear stress; WSSsec – Secondary wall shear stress; WSŜsec – Normalised secondary wall shear stress; Div – WSS divergence; TSVI – Topological shear variation index.

Table 6
Intraclass correlation coefficients (r; p-value) between TAWSS and other WSS metrics in patient specific CFD, static FSI (FSI-S) and dynamic FSI (FSI-D) simulations. Bold values highlight relationships that are *not* significant ($p>0.05$). Highlighted cells show relationships that have a weak correlation coefficient ($-0.5<r<0.5$), suggesting outside influences or nonlinearity of the relationship. Abbreviations as in Table 4 and 5.

		OSI	RRT	TrWSS	CFI	WSSax	WSŜaxe	WSSsec	*WSŜsec*	Div	TSVI	CP
TAWSS	CFD	−0.78; $p<0.001$	−0.98; $p<0.001$	−0.087; $p<0.001$	−0.19; $p<0.001$	0.99; $p<0.001$	0.71; $p<0.001$	−0.11; $p<0.001$	0.0010; $p=0.95$	−0.030; $p=0.097$	−0.69; $p<0.001$	−0.047; $p<0.01$
	FSI-S	−0.79; $p<0.001$	−0.97; $p<0.001$	−0.18; $p<0.001$	−0.22; $p<0.001$	0.99; $p<0.001$	0.70; $p<0.001$	−0.069; $p<0.001$	0.10; $p<0.001$	0.040; $p=0.024$	−0.73; $p<0.001$	−0.15; $p<0.001$
	FSI-D	−0.80; $p<0.001$	−0.98; $p<0.001$	−0.27; $p<0.001$	−0.28; $p<0.001$	0.99; $p<0.001$	0.73; $p<0.001$	−0.11; $p<0.001$	0.14; $p<0.001$	0.13; $p<0.001$	−0.70; $p<0.001$	−0.16; $p<0.001$

Table 7
Interclass correlation coefficients (r; p-value) between WSS derived metrics in CFD, static FSI (FSI-S) and dynamic FSI (FSI-D) simulations. Bold values show significant ($>10\%$) change in correlation coefficient with varied FSI boundary conditions. Abbreviations as in Table 4 and 5.

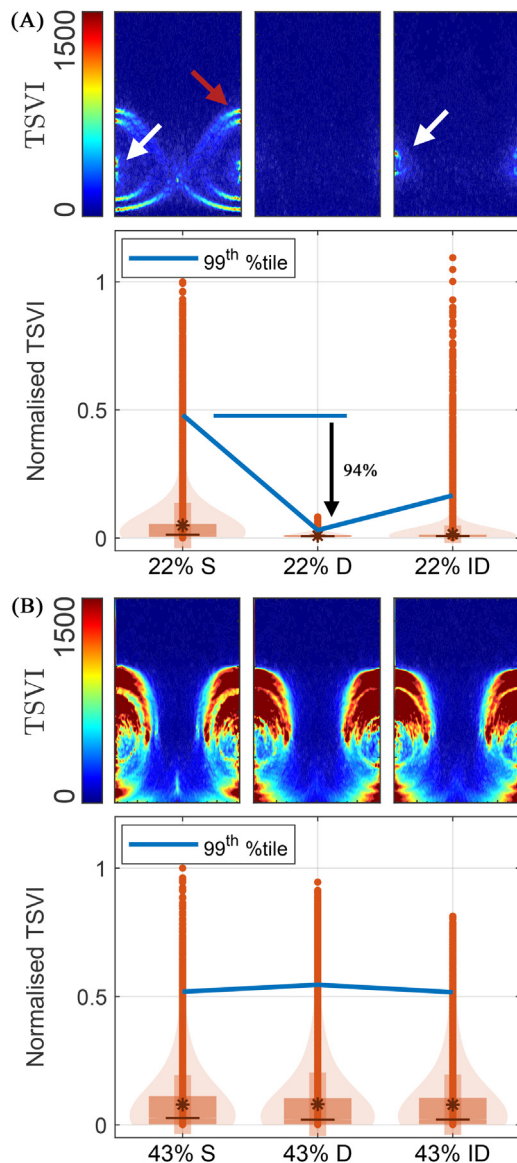|	WSS derived metric (CFD)											
	TAWSS	OSI	RRT	TrWSS	CFI	WSSax	WSŜaxe	WSSsec	*WSŜsec*	Div	TSVI	CP
FSI-S	0.89; $p<0.001$	0.87; $p<0.001$	0.88; $p<0.001$	0.79; $p<0.001$	0.60; $p<0.001$	0.89; $p<0.001$	0.89; $p<0.001$	0.91; $p<0.001$	0.91; $p<0.001$	0.80; $p<0.001$	0.80; $p<0.001$	0.21; $p<0.001$
FSI-D	0.88; $p<0.001$	0.76; $p<0.001$	0.87; $p<0.001$	0.47; $p<0.001$	0.56; $p<0.001$	0.88; $p<0.001$	0.87; $p<0.001$	0.86; $p<0.001$	0.86; $p<0.001$	0.74; $p<0.001$	0.74; $p<0.001$	0.16; $p<0.001$

Fig. 16. TSVI at 22% stenosis (A) and 43% stenosis (B). Dynamic boundary conditions play a significant role at in smaller stenosis, reducing the 99th percentile by 94%. Violin plots are normalised against the static simulation maximums for visualisation purposes. S – Static FSI; D – Dynamic FSI; ID – Inverse Dynamic FSI.

Fig. 17. Association between the twelve WSS-based metrics and vessel remodelling, measured as the change in lumen area. Outer ring: Locally weighted, non-parametric logistic regression (LOESS) plots with 95% confidence intervals for each of the three simulations against vessel remodelling, where the red arrows show reducing lumen area (negative remodelling) and the green arrows show increasing lumen area (positive remodelling). Inner ring: Welch's t-test results, describing the strength of the difference between mean values in areas of positive and negative remodelling. The baseline result for TAWSS is plotted as a ring for comparison. Linear correlation coefficients (R^2) are shown to demonstrate how the relationship changes with differing simulations.

ation given non-atherosclerotic (and younger) vessels are significantly more compliant than diseased ones, potentially exacerbating the impact of dynamics and FSI couplings. While this is by no means concrete evidence for the role of dynamics in the developmental stages of diseases, is does warrant further investigation in the future. However, we did not vary the displacement magnitude nor the gradient of dynamic changes in this study, which could exacerbate the changes we presented here. From our results we hypothesise that larger dynamical magnitudes and gradients will alter WSS topology more significantly, potentially amplifying the associations with vessel remodelling and lesion changes. Future studies could investigate these changes to determine if there is a critical point beyond which these dynamic effects may be compounded. Furthermore, we did not assess the impact of coronary bending/torsion or variations in the overall rigid-body displacement profile. Our idealised models also varied only two geometrical factors: stenosis severity and lesion length. These factors can vary significantly between patients, limiting the generalisability of our results and warrant more detailed future investigations. It appears likely that these factors will increase the ef-
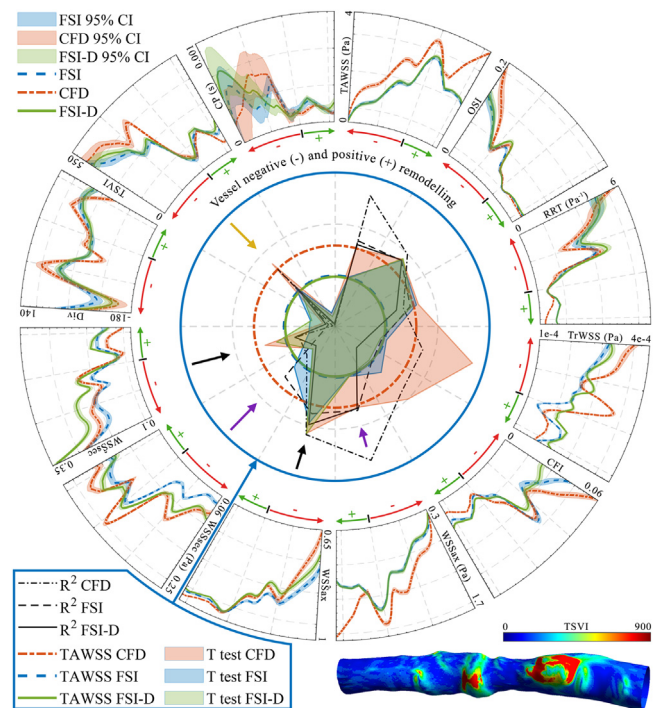
fective stenosis level of some lesions, potentially amplifying the multi-directional/topological effect of only mild lesions, resulting in marked changes in WSS topology which require further investigation.

We also raised in the methodology our assumption that normal near-wall velocity components introduced through the FSI coupling and dynamics are sufficiently small as to not impact divergence calculations. This assumption is unproven but based on knowledge that the normal near-wall velocity component has been demonstrated as much smaller than tangential components and can therefore be assumed as negligible. This also leads to further commonly held assumptions that do not necessarily hold in biological simulations, namely, the no-slip condition at the fluid-solid interface (i.e. a sufficiently smooth wall), in conjunction with no wall penetration/transport and a continuous fluid [26,91]. In reality the vessel wall is a rough surface due to small grooves in the cellular substrate and blood is not continuous as it contains discrete constituents (red blood cells etc.) suspended in plasma which can penetrate the vessel walls [12], of which the blood-wall coupling has been suggested to impact [92]. It has already been shown that the surface roughness of blood vessels impacts WSS and the microscale, with larger WSS variability than smooth walls [93]. When also considering slip is an important factor in rough walled models, and is dependant on both shear and normal stress, this draws into question the expansion of near-wall velocity from the shear stress vector alone, the backbone of the presented topological calculations, which also requires further rigorous mathematical investigation [86,94]. This also raises the need for further experimental microfluidic investigations that can culture cellular substrates in controlled flow conditions to better validate mathematical models and understand the biological significance of each of the multi-

directional/topological metrics assessed throughout this work. This is particularly relevant to the results from Fig. 9a and Appendix A2, relating to the critical point locations over the cardiac cycle. If a critical point location is always a critical point throughout the cardiac cycle, then multidirectional metrics such as OSI have no physical meaning, which calls into question their biological relevance [33].

This investigation also focused substantially on time averaged measures (except for the TSVI and CP residence time). The results from the idealised simulations showed that while time averaged WSS divergence did not see significant changes, the TSVI could be altered by coronary dynamics. This highlights the importance of investigating the transient nature of coronary flow in tandem with coronary dynamics. We strongly suggest that variation indices be developed for other multi-directional/topological and intraluminal flow markers to understand how they vary over each cardiac cycle. The transient nature of coronary flow under varying blood velocity and pressure profiles could also be further explored, with the prevalence of the backward propagating pressure pulses in the coronary vasculature showing potentially important impacts on these results.

Our numerical setup was also limited to a single layered, orthotropic hyperelastic material model which used the principal axial and circumferential directions for fibre orientation. Future studies could make use of the more complete anisotropic models presented in [57,95], as well as multiple artery layers and differing properties for the lesion's fibrous cap, whose stiffness could be significantly greater than what we presented in this work. This is an important consideration for interpreting our results, as a stiffer wall could be considered to act more closely to the rigid-walled CFD simulations, suggesting our results and their interpretations as an upper bound on potential differences. The idealised geometry used to parametrically study dynamic effects could be expanded to include artery taper, curvature and bifurcation regions to determine how dynamics and fully-coupled FSI could affect WSS topology in a wider range of morphological settings [96]. Such investigations could also make use of laminar flow conditions to prevent the inclusion of the additional assumptions brought on with the Reynolds-averaged Navier Stokes equations, a limitation in the current study. Furthermore, studies have suggested that stenosis percentage alone is insufficient to quantify risks to coronary plaque, with irregular lumen surfaces, stenosis aspect ratio, eccentricity and pulsatile flow all impacting risk factors [49,97–99]. Hence, further studies are encouraged to quantify how the relationships presented in this work may vary under changes in these factors.

The patient-specific simulations were also limited through their use of the same numerical setup as the parametric study. While artery properties cannot currently be determined *in vivo*, future studies must focus on developing pathways to tailor these properties to better resemble patient conditions. Furthermore, the velocity and pressure profiles were the same in both the patient and idealised cases. Future work must apply patient-specific flow conditions to accurately model patient-specific WSS multi-directional/topological [100]. Our geometry reconstruction was a predominantly manual process subject to interobserver variability. Further work must be undertaken to automate this process for a robust and repeatable reconstruction that can also consider branch regions which have already been shown to significantly impact WSS results [101,102]. Another limitation, for simplicity, was that we only assessed differences in WSS metrics in regions that saw either an increase or decrease in each respective morphological factor (lumen area, lipid arc, fibrous cap thickness). Further work is required to determine if the changes we presented here are consistent across varying degrees of remodelling and plaque composition variations. Finally, our focus has been on twelve WSS metrics but did not include Lagrangian approaches, such as the WSS exposure time presented in [29], due to the added computation cost of seeding tracers on a sufficiently fine mesh and computing over multiple cardiac cycles. Our future studies will look to include this approach with FSI simulations while addressing the relationships with the twelve WSS metrics assessed here.

Our patient-specific simulations are also limited to only one example patient model, preventing results from being generalised. There is a clear need to determine if these changes between CFD- and FSI-based studies hold for larger, longitudinal cohort studies and how these approaches may alter our ability to predict changes in the coronary vasculature. This raises the issue of clinical translation, which requires threshold values for multidirectional/topological WSS metrics to be applied in clinical decision making, something recent topological studies begin to present [36,37]. For such computations to take place, near-real time results are required. This brings into question the need for more complex and computationally expensive simulations such as the approaches we discuss. Acknowledging this, instead we see the need for added computational rigour to determine the fundamental biological links between multi-directional/topological WSS, factors that impact their computation, and the natural history of atherosclerosis so that the most effective haemodynamic metrics can be targeted. From this rigour, computationally simpler approaches, such as reduced order modelling already applied quantitative flow reserve computations or machine learning approaches, could be extended to determine these transient and multi-directional properties within the necessary time frames to both make larger cohort studies and real-world use more practical [103,104].

5. Conclusion

In this paper the relationships between twelve multidirectional/topological WSS metrics and the influence of stenosis percentage, lesion length, FSI simulation and coronary dynamics in both idealised and patient-specific cases has been investigated. Our results highlight the nonlinear relationship between stenosis percentage, lesion length and all WSS metrics. 22–32% stenosis appears as the critical threshold level beyond which adverse and multi-directional WSS properties are amplified, with 25% stenosis being the point of inflection where attracting WSS divergence strength imbalances the repelling strength. FSI alone produces small alterations in WSS metrics; however, the addition of coronary dynamics produces more significant alterations in the directional properties of the WSS vector. These changes appear most critically at smaller stenosis levels, suggesting coronary dynamics could play a role in the earlier stages of atherosclerosis development. Finally, our patient specific case comparison shows that WSS direction can be influenced by coronary dynamics, which impacts the associations between each metric and vessel remodelling and plaque morphology changes in line with idealised results. This now raises a further question on whether these subtle variations could alter associations and prognostic value of WSS metrics with changes in coronary atherosclerosis over time, warranting further investigation in a wider range of morphological settings and longitudinal cohort studies in the future.

Compliance with ethical standards

This study was carried out with permission from the Central Adelaide Local Health Network (CALHN) Research Services (CALHN Reference Number 14179) for biomechanical simulations after the patient was recruited into the ongoing colchicine for coronary plaque modification in acute coronary syndrome (COCOMO-ACS) randomized-controlled trial (ACTRN12618000809235; Royal Adelaide Hospital HREC reference number: HREC/17/RAH/366).

Declaration of Competing Interest

Acknowledgements

Supplementary materials

Supplementary material associated with this article can be found, in the online version, at doi:10.1016/j.cmpb.2023.107418.

Appendix A1. FSI and CFD scaling coefficients

Table A1 outlines the correlation coefficient and the parameters for a linear fit between FSI and CFD simulation data, as described in Eq. 15.

$$FSI = a.CFD + b \qquad (15)$$

Appendix A2. A note on the equivalence of divergence and critical point calculations

In Eq. (8), we take the integral over the cardiac cycle of the scalar divergence computed using the instantaneous, normalized WSS vector field. This is *not* necessarily equivalent to taking the scalar divergence of the normalised TAWSS vector field previously described as [33]

$$\nabla \cdot \frac{\boldsymbol{\tau}_{TAWSS}(\mathbf{p}, t)}{\|\boldsymbol{\tau}_{TAWSS}(\mathbf{p}, t)\|} dt = \nabla \boldsymbol{\tau}_{TAWSSx}(\mathbf{p}, t) \cdot \hat{\mathbf{x}} + \nabla \boldsymbol{\tau}_{TAWSSy}(\mathbf{p}, t) \cdot \hat{\mathbf{y}}$$
$$+ \nabla \boldsymbol{\tau}_{TAWSSz}(\mathbf{p}, t) \cdot \hat{\mathbf{z}} dt. \qquad (16)$$

Normalising the vector field at each time step allows us to investigate in greater detail the multi-directional properties of the WSS vector field, without the impact of its magnitude. By doing so, each time-step in the time-integral from Eq. (8) is effectively equally weighted (no impact from WSS magnitude), altering the cycle-averaged divergence scalar field when compared to using only the single vector field of the TAWSS which is then normalised *after* its time-average is taken. In more detail, if we first take the integral of the WSS vector field over the time a to b (i.e. the TAWSS vector field for the cardiac cycle when a-b=T) as,

$$\frac{1}{(b-a)} \int_a^b \boldsymbol{\tau}(\mathbf{p}, t) dt, \qquad (17)$$

where $\mathbf{p}$ is a position vector ($\boldsymbol{p}$= $[x, y, z]$). We can then express its partial derivative with respect to an arbitrary coordinate via Leibniz's integral rule. For simplicity, taking the partial derivative with respect to the x coordinate, we have

$$\frac{1}{(b-a)} \frac{\partial}{\partial x} \left(\int_a^b \boldsymbol{\tau}(\mathbf{p}, t) dt \right) = \frac{1}{(b-a)} \left(\boldsymbol{\tau}(\mathbf{p}, b) \frac{\partial}{\partial x} b - \boldsymbol{\tau}(\mathbf{p}, a) \frac{\partial}{\partial x} a \right)$$

$$+ \int_a^b \frac{\partial}{\partial x} \boldsymbol{\tau}(\mathbf{p}, t) dt \bigg), \qquad (18)$$

which can then be simplified when a and b are constants (i.e., time) to

$$\frac{\partial}{\partial x} \left(\int_a^b \boldsymbol{\tau}(\mathbf{p}, t) dt \right) = \int_a^b \frac{\partial}{\partial x} \boldsymbol{\tau}(\mathbf{p}, t) dt. \qquad (19)$$

This is then easily expanded to include the partial derivatives in the y and z orientations. As the del operator, ∇, is a vector of partial derivatives,

$$\nabla = \left(\frac{\partial}{\partial x}, \frac{\partial}{\partial y}, \frac{\partial}{\partial z} \right), \qquad (20)$$

and the divergence is the dot product between the del operator and a specified vector field, by extension Eq. (19) states that the divergence of the TAWSS vector field is equivalent to the time averaged divergence of the WSS vector field. This is due to the limits of integration being time-dependant scalars, not position dependant, allowing the divergence (partial derivatives) operator to come outside of the integral and the remaining terms to become zero.

However, when we are dealing with the normalised vector field there is a significant difference. Mathematically, this difference becomes obvious through use of the triangle inequality (or integral inequality) applied over the WSS vector field for a cardiac cycle, T, which by induction states

$$\left\| \int_o^T \boldsymbol{\tau}(t) \right\| \leq \int_0^T \|\boldsymbol{\tau}(t)\|, \qquad (21)$$

and, therefore, implies

$$\nabla \cdot \frac{\int_0^T \boldsymbol{\tau}_i}{\left\| \int_0^T \boldsymbol{\tau}_i \right\|} \neq \int_0^T \nabla \cdot \frac{\boldsymbol{\tau}_i}{\|\boldsymbol{\tau}_i\|}. \qquad (22)$$

It should also be noted that the divergence of the normalised cycle averaged WSS vector field and the time-averaged divergence of the normalised WSS vector field can still be equivalent in regions that do not exhibit flow reversal. As has been previously highlighted, this calls into question the physiological meaning of multi-directional flow metrics in these regions [33]. These differences have been demonstrated using the resulting WSS vector field from the 43% stenosis model (CFD simulation) in Fig. 18.

Importantly, this approach allows us to investigate how the pulsatile flow conditions impact multi-directional WSS over the different phases of the cardiac cycle. For instance, the contraction of the myocardium during the systolic phase leads to the most significant motion/torsion/bending over this time, when blood velocity in the left anterior descending artery is suppressed by microcirculatory resistance. Typically, the higher blood velocity over the diastolic phase overpowers the impact of the systolic phase on WSS magnitude, missing what could be important variations. Of course, in the case of other vessels such as the right coronary artery, blood velocity over the systolic phase is not suppressed in the same manner so different outcomes could be expected. This still requires further investigation.

Furthermore, this approach allows us to quantify critical point locations at every timepoint over the cardiac cycle, avoiding the paradoxical results previously highlighted that suggested a critical point at a location in the normalised TAWSS vector field may never actually be a critical point in the time-dependant WSS vector field [33]. Again, this is demonstrated in Fig. 18. However, the physiological significance of this is still not understood [84].

Table A1
Linear fits between CFD and FSI simulations, with either static or dynamic FSI boundary conditions. *Dynamic relationship is influenced by displacement direction.

|		Idealised 22% stenosis 18 mm lesion length			43% stenosis 18 mm lesion length			43% stenosis 10 mm lesion length			Patient- Specific Case		
		R^2	a	b	R^2	a	b	R^2	a	b	R^2	a	b
TAWSS	Static	0.99	0.58	0.073	0.99	0.62	0.42	0.98	0.59	−0.058	0.78	0.60	0.18
	Dynamic*	0.99	0.58	0.074	0.99	0.59	0.24	0.98	0.59	−0.065	0.77	0.63	0.14
OSI	Static	0.93	1.47	−1.14e-6	0.77	0.10	8.45e-5	0.65	0.81	0.015	0.75	0.75	0.0035
	Dynamic*	0.92	1.01	−2.96e-7	0.96	0.41	8.92e-6	0.64	0.73	0.014	0.81	0.72	0.0024
RRT	Static	0.99	1.63	0.011	0.97	1.05	0.068	0.13	0.72	1.11	0.69	1.14	0.13
	Dynamic*	0.99	1.64	0.0097	0.99	1.26	0.058	0.25	0.65	1.14	0.85	1.10	0.22
TrWSS	Static	0.89	0.64	8.56e-6	0.21	0.37	5.44e-5	0.71	0.84	1.86e-4	0.52	0.51	7.77e-5
	Dynamic*	0.79	0.31	2.22e-6	0.85	0.54	−4.5e-6	0.73	0.69	1.25e-4	0.052	0.17	2.26e-4
CFI	Static	0.87	0.99	6.35e-5	0.62	0.29	9.02e-4	0.57	1.06	0.020	0.52	0.79	0.0036
	Dynamic*	0.83	0.61	4.41e-6	0.95	0.64	−1.11e-4	0.65	0.96	0.012	0.43	0.68	0.0060
WSSax	Static	0.99	0.58	0.069	0.99	0.62	0.42	0.98	0.59	−0.11	0.79	0.60	0.17
	Dynamic*	0.99	0.58	0.055	0.99	0.59	0.23	0.98	0.59	−0.12	0.79	0.64	0.12
WSŜaxe	Static	0.86	1.52	−0.52	0.79	0.20	0.80	0.96	0.91	0.022	0.87	0.67	0.31
	Dynamic*	0.35	3.79	−2.79	0.94	0.54	0.46	0.96	0.93	−0.0084	0.88	0.83	0.15
WSSsec	Static	0.97	0.56	−6.89e-6	0.68	0.53	−3.84e-4	0.68	0.69	−3.13e-4	0.86	0.72	3.11e-4
	Dynamic*	0.97	1.33	1.97e-4	0.97	0.39	3.81e-4	0.68	0.69	−2.62e-4	0.84	0.80	−0.0024
WSŜsec	Static	0.97	0.98	8.51e-8	0.019	0.16	4.58e-4	0.89	1.24	−7.02e-4	0.83	0.82	−0.023
	Dynamic*	0.97	2.46	1.75e-4	0.96	0.64	1.74e-4	0.87	1.29	−8.02e-4	0.81	0.97	−0.033
Divergence	Static	0.52	0.67	7.61	0.080	0.22	43.32	0.56	0.61	−0.39	0.54	0.59	−6.99
	Dynamic*	0.53	0.69	7.27	0.75	0.65	24.36	0.59	0.66	−1.36	0.54	0.67	−3.94
TSVI	Static	0.15	0.45	5.01	0.67	0.43	40.52	0.69	0.69	109.55	0.46	0.72	52.70
	Dynamic*	0.15	0.36	4.92	0.86	0.76	−6.86	0.77	0.71	67.15	0.48	0.74	56.72
CP	Static	0.0	1.00	0.00	0.031	0.081	4.00e-5	0.094	0.67	2.97e-4	0.14	2.05	7.91e-5
	Dynamic*	0.0	1.00	0.00	0.81	0.45	−1.39e-8	0.12	0.68	2.18e-4	0.11	1.48	4.16e-5
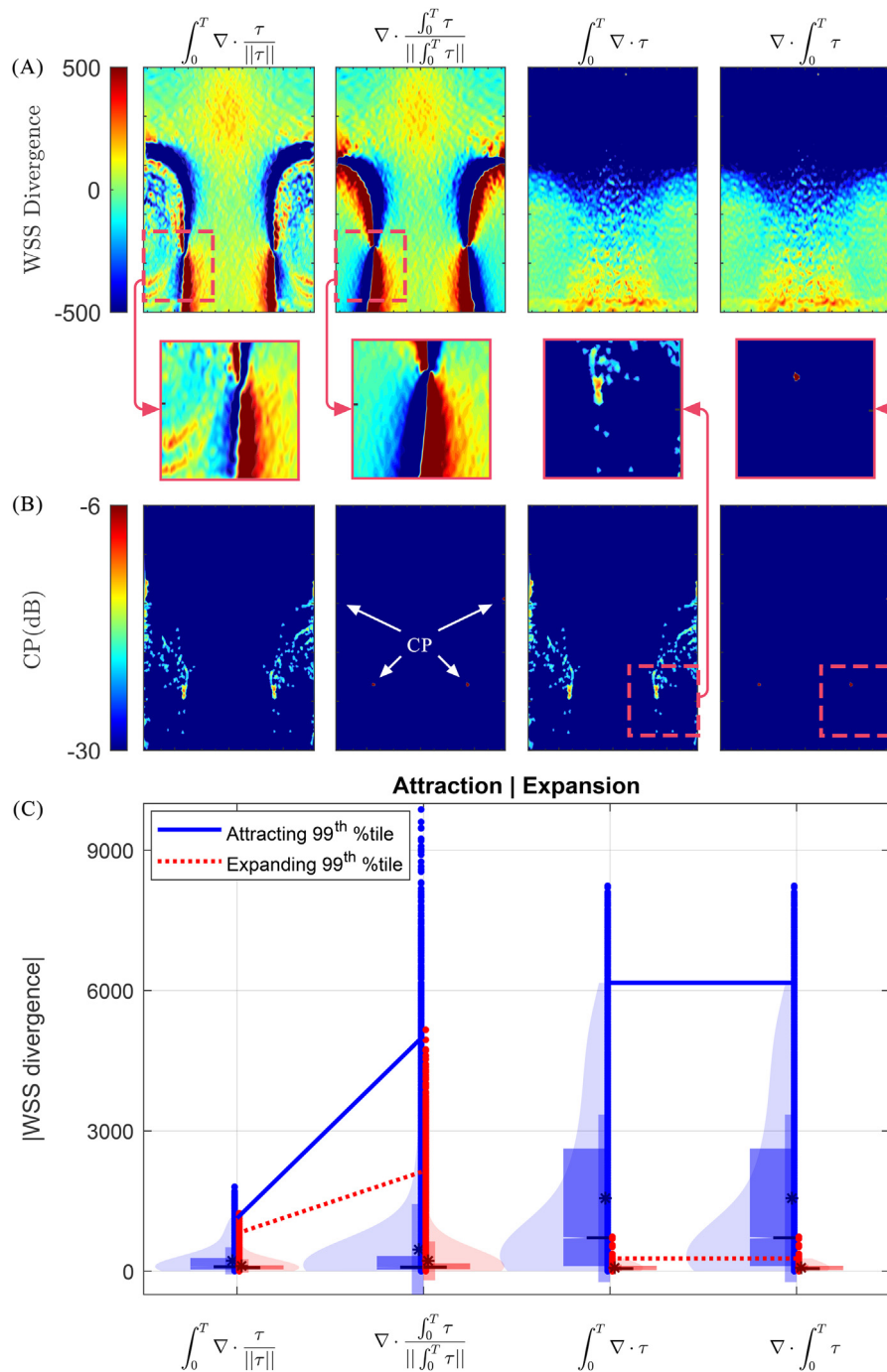
Fig. 18. Comparison of various approaches to computing the WSS divergence and the use of instantaneous vs time-averaged WSS vector field for critical point location computation in the 43% stenosis model. (A) Visualisation of results from divergence calculation. Note the subtle differences, inset, which stem from the TAWSS being unable to capture how WSS topology changes over the cardiac cycle (further visualisation of this is provided in Fig. 9A). (B) Critical point locations, where the critical point located in the TAWSS vector field corresponds to the largest critical point residence time in the transient WSS vector field. (C) Absolute values of divergence (attracting and expanding regions) demonstrating the inequality in the use of the normalised vector field and equality for the non-normalised vector field.

References

[1] A. Gheorghe, U. Griffiths, A. Murphy, H. Legido-Quigley, P. Lamptey, P. Perel, The economic burden of cardiovascular disease and hypertension in low-and middle-income countries: a systematic review, BMC Public Health 18 (1) (2018) 1–11.

[2] R.W. Yeh, S. Sidney, M. Chandra, M. Sorel, J.V. Selby, A.S. Go, Population trends in the incidence and outcomes of acute myocardial infarction, N. Engl. J. Med. 362 (23) (2010) 2155–2165.

[3] A.A.W. Baumann, R. Tavella, T.M. Air, A. Mishra, N.J. Montarello, M. Arstall, C. Zeitz, M.I. Worthley, J.F. Beltrame, P.J. Psaltis, Prevalence and real-world management of NSTEMI with multivessel disease, Cardiovasc. Diagn. Ther. 12 (1) (2022) 1–11.

[4] M. Emond, M.B. Mock, K.B. Davis, L.D. Fisher, D.R. Holmes Jr., B.R. Chaitman, G.C. Kaiser, E. Alderman, T. Killip, Long-term survival of medically treated patients in the coronary artery surgery study (CASS) registry, Circulation 90 (6) (1994) 2645–2657.

[5] G.A. Figtree, S.T. Vernon, N. Hadziosmanovic, J. Sundström, J. Alfredsson, S.J. Nicholls, C.K. Chow, P. Psaltis, H. Røsjø, M. Leósdóttir, E. Hagström, Mortality and cardiovascular outcomes in patients presenting with non–ST elevation myocardial infarction despite no standard modifiable risk factors: results from the swedeheart registry, J. Am. Heart Assoc. 11 (15) (2022) e024818.

[6] A.A.W. Baumann, A. Mishra, M.I. Worthley, A.J. Nelson, P.J. Psaltis, Manage-

ment of multivessel coronary artery disease in patients with non-ST-elevation myocardial infarction: a complex path to precision medicine, Ther. Adv. Chronic. Dis. 11 (2020) 1–23.

[7] A.J. Nelson, M. Ardissino, P. Psaltis, Current approach to the diagnosis of atherosclerotic coronary artery disease: more questions than answers, Ther. Adv. Chronic. Dis. 10 (2019) 1–20.

[8] G.W. Stone, A. Maehara, A.J. Lansky, B. de Bruyne, E. Cristea, G.S. Mintz, R. Mehran, J. McPherson, N. Farhat, S.P. Marso, H. Parise, B. Templin, R. White, Z. Zhang, P.W. Serruys, A prospective natural-history study of coronary atherosclerosis, N. Engl. J. Med. 364 (3) (2011) 226–235.

[9] Y. Cai, Z. Li, Mathematical modeling of plaque progression and associated microenvironment: how far from predicting the fate of atherosclerosis? Comput. Methods Programs Biomed. 211 (2021) 106435.

[10] H.J. Carpenter, A. Gholipour, M.H. Ghayesh, A.C. Zander, P.J. Psaltis, A review on the biomechanics of coronary arteries, Int. J. Eng. Sci. 147 (2020) 1–62.

[11] J.V. Soulis, D.K. Fytanidis, V.C. Papaioannou, G.D. Giannoglou, Wall shear stress on LDL accumulation in human RCAs, Med. Eng. Phys. 32 (8) (2010) 867–877.

[12] M. Mahmoudi, A. Farghadan, D. McConnell, A.J. Barker, J.J. Wentzel, M.J. Budoff, A. Arzani, The story of wall shear stress in coronary artery atherosclerosis: biochemical transport and mechanotransduction, J. Biomech. Eng. 143 (8) (2020).

[13] S. Chatzizisis Yiannis, U. Coskun Ahmet, M. Jonas, R. Edelman Elazer, L. Feldman Charles, H. Stone Peter, Role of endothelial shear stress in the natural history of coronary atherosclerosis and vascular remodeling, J. Am. Coll. Cardiol. 49 (25) (2007) 2379–2393.

[14] L. Xia, B. Zhang, Y. Sun, B. Chen, Z. Yu, Analysis of Syk/PECAM-1 signaling pathway in low shear stress induced atherosclerosis based on ultrasound imaging, Comput. Methods Programs Biomed. 201 (2021) 105953.

[15] Y. Sun, B. Zhang, L. Xia, Effect of low wall shear stress on the morphology of endothelial cells and its evaluation indicators, Comput. Methods Programs Biomed. 208 (2021) 106082.

[16] P.H. Stone, A. Maehara, A.U. Coskun, C.C. Maynard, M. Zaromytidou, G. Siasos, I. Andreou, D. Fotiadis, K. Stefanou, M. Papafaklis, L. Michalis, A.J. Lansky, G.S. Mintz, P.W. Serruys, C.L. Feldman, G.W. Stone, Role of low endothelial shear stress and plaque characteristics in the prediction of nonculprit major adverse cardiac events: the PROSPECT study, JACC Cardiovasc. Imaging 11 (3) (2018) 462–471.

[17] P.H. Stone, S. Saito, S. Takahashi, Y. Makita, S. Nakamura, T. Kawasaki, A. Takahashi, T. Katsuki, S. Nakamura, A. Namiki, Prediction of progression of coronary artery disease and clinical outcomes using vascular profiling of endothelial shear stress and arterial plaque characteristics: the PREDICTION study, Circulation 126 (2) (2012) 172–181.

[18] V. Bourantas Christos, T. Zanchin, R. Torii, W. Serruys Patrick, A. Karagiannis, A. Ramasamy, H. Safi, U. Coskun Ahmet, G. Koning, Y. Onuma, C. Zanchin, R. Krams, A. Mathur, A. Baumbach, G. Mintz, S. Windecker, A. Lansky, A. Maehara, H. Stone Peter, L. Raber, W. Stone Gregg, Shear stress estimated by quantitative coronary angiography predicts plaques prone to progress and cause events, JACC Cardiovasc. Imaging 13 (10) (2020) 2206–2219.

[19] J.C. Tremblay, T.V. Stimpson, K.E. Pyke, Evidence of sex differences in the acute impact of oscillatory shear stress on endothelial function, J. Appl. Physiol. 126 (2) (2019) 314–321.

[20] A.S. Storch, H.N.M. Rocha, V.P. Garcia, G.M. da Silva Batista, J.D. Mattos, M.O. Campos, A.L. Fuly, A.C.L. da Nóbrega, I.A. Fernandes, N.G. Rocha, Oscillatory shear stress induces hemostatic imbalance in healthy men, Thromb. Res. 170 (2018) 119–125.

[21] Y. Mohamied, S.J. Sherwin, P.D. Weinberg, Understanding the fluid mechanics behind transverse wall shear stress, J. Biomech. 50 (2017) 102–109.

[22] V. Peiffer, S.J. Sherwin, P.D. Weinberg, Computation in the rabbit aorta of a new metric – the transverse wall shear stress – to quantify the multidirectional character of disturbed blood flow, J. Biomech. 46 (15) (2013) 2651–2658.

[23] A. Hoogendoorn, A.M. Kok, E.M.J. Hartman, G. De Nisco, L. Casadonte, C. Chiastra, A. Coenen, S.A. Korteland, K. Van der Heiden, F.J.H. Gijsen, D.J. Duncker, A.F.W. Van der Steen, J.J. Wentzel, Multidirectional wall shear stress promotes advanced coronary plaque development: comparing five shear stress metrics, Cardiovasc. Res. 116 (6) (2020) 1136–1146.

[24] U. Morbiducci, D. Gallo, S. Cristofanelli, R. Ponzini, M.A. Deriu, G. Rizzo, D.A. Steinman, A rational approach to defining principal axes of multidirectional wall shear stress in realistic vascular geometries, with application to the study of the influence of helical flow on wall shear stress directionality in aorta, J. Biomech. 48 (6) (2015) 899–906.

[25] G. De Nisco, A.M. Kok, C. Chiastra, D. Gallo, A. Hoogendoorn, F. Migliavacca, J.J. Wentzel, U. Morbiducci, The atheroprotective nature of helical flow in coronary arteries, Ann. Biomed. Eng. 47 (2) (2019) 425–438.

[26] A. Arzani, A.M. Gambaruto, G. Chen, S.C. Shadden, Lagrangian wall shear stress structures and near-wall transport in high-Schmidt-number aneurysmal flows, J. Fluid Mech. 790 (2016) 158.

[27] S.C. Shadden, C.A. Taylor, Characterization of coherent structures in the cardiovascular system, Ann. Biomed. Eng. 36 (2008) 1152–1162.

[28] S.C. Shadden, A. Arzani, Lagrangian postprocessing of computational hemodynamics, Ann. Biomed. Eng. 43 (2015) 41–58.

[29] A. Arzani, A.M. Gambaruto, G. Chen, S.C. Shadden, Wall shear stress exposure time: a Lagrangian measure of near-wall stagnation and concentration in cardiovascular flows, Biomech. Model. Mechanobiol. 16 (3) (2017) 787–803.

[30] A. Arzani, S.C. Shadden, Wall shear stress fixed points in cardiovascular fluid mechanics, J. Biomech. 73 (2018) 145–152.

[31] J. Martorell, P. Santoma, K. Kolandaivelu, V.B. Kolachalama, P. Melgar-Lesmes, J.J. Molins, L. Garcia, E.R. Edelman, M. Balcells, Extent of flow recirculation governs expression of atherosclerotic and thrombotic biomarkers in arterial bifurcations, Cardiovasc. Res. 103 (1) (2014) 37–46.

[32] J.L. Zhao, L. Jia, X.B. Wang, L.L. Zhang, W.L. Rong, J.W. Jiang, M.H. Li, Effects of adjustable impinging flow on the vascular endothelial cell layer in a modified T chamber, Int. J. Clin. Exp. Med. 10 (3) (2017) 5068–5074.

[33] V. Mazzi, D. Gallo, K. Calò, M. Najafi, M.O. Khan, G. De Nisco, D.A. Steinman, U. Morbiducci, A Eulerian method to analyze wall shear stress fixed points and manifolds in cardiovascular flows, Biomech. Model. Mechanobiol. 19 (5) (2020) 1403–1423.

[34] G. De Nisco, P. Tasso, K. Calò, V. Mazzi, D. Gallo, F. Condemi, S. Farzaneh, S. Avril, U. Morbiducci, Deciphering ascending thoracic aortic aneurysm hemodynamics in relation to biomechanical properties, Med. Eng. Phys. 82 (2020) 119–129.

[35] U. Morbiducci, V. Mazzi, M. Domanin, G. De Nisco, C. Vergara, D.A. Steinman, D. Gallo, Wall shear stress topological skeleton independently predicts long-term restenosis after carotid bifurcation endarterectomy, Ann. Biomed. Eng. 48 (12) (2020) 2936–2949.

[36] V. Mazzi, G. De Nisco, A. Hoogendoorn, K. Calò, C. Chiastra, D. Gallo, D.A. Steinman, J.J. Wentzel, U. Morbiducci, Early Atherosclerotic Changes in Coronary Arteries are Associated with Endothelium Shear Stress Contraction/Expansion Variability, Ann. Biomed. Eng. 49 (9) (2021) 2606–2621.

[37] A. Candreva, M. Pagnoni, M.L. Rizzini, T. Mizukami, E. Gallinoro, V. Mazzi, D. Gallo, D. Meier, T. Shinke, J.P. Aben, S. Nagumo, J. Sonck, D. Munhoz, S. Fournier, E. Barbato, W. Heggermont, S. Cook, C. Chiastra, U. Morbiducci, B. De Bruyne, O. Muller, C. Collet, Risk of myocardial infarction based on endothelial shear stress analysis using coronary angiography, Atherosclerosis 342 (2022) 28–35.

[38] H. Carpenter, A. Gholipour, M. Ghayesh, A.C. Zander, P. Psaltis, *In vivo* based fluid-structure interaction biomechanics of the left anterior descending coronary artery, J. Biomech. Eng. 143 (8) (2021) 1–18.

[39] D. Tang, C. Yang, S. Kobayashi, J. Zheng, P.K. Woodard, Z. Teng, K. Billiar, R. Bach, D.N. Ku, 3D MRI-based anisotropic FSI models with cyclic bending for human coronary atherosclerotic plaque mechanical analysis, J. Biomech. Eng. 131 (6) (2009) 1–11.

[40] M. Malvè, A. García, J. Ohayon, M.A. Martínez, Unsteady blood flow and mass transfer of a human left coronary artery bifurcation: FSI vs. CFD, Int. Commun. Heat Mass Transf. 39 (6) (2012) 745–751.

[41] J. Dong, Z. Sun, K. Inthavong, J. Tu, Fluid–structure interaction analysis of the left coronary artery with variable angulation, Comput. Methods Biomech. Biomed. Eng. 18 (14) (2015) 1500–1508.

[42] M. Cilla, I. Borrás, E. Peña, M.A. Martínez, M. Malvè, A parametric model for analysing atherosclerotic arteries: on the FSI coupling, Int. Commun. Heat Mass Transf. 67 (2015) 29–38.

[43] P.A.L. Tonino, B. De Bruyne, N.H.J. Pijls, U. Siebert, F. Ikeno, M. Van 't Veer, V. Klauss, G. Manoharan, T. Engstrøm, K.G. Oldroyd, P.N. Ver Lee, P.A. MacCarthy, W.F. Fearon, Fractional flow reserve versus angiography for guiding percutaneous coronary intervention, N. Engl. J. Med. 360 (3) (2009) 213–224.

[44] P.A. Tonino, W.F. Fearon, B. De Bruyne, K.G. Oldroyd, M.A. Leesar, P.N. Ver Lee, P.A. MacCarthy, M. Van't Veer, N.H. Pijls, Angiographic versus functional severity of coronary artery stenoses in the FAME study: fractional flow reserve versus angiography in multivessel evaluation, J. Am. Coll. Cardiol. 55 (25) (2010) 2816–2821.

[45] A. Ahmadi, G.W. Stone, J. Leipsic, P.W. Serruys, L. Shaw, H. Hecht, G. Wong, B.L. Nørgaard, P.T. O'Gara, Y. Chandrashekhar, J Narula, Association of coronary stenosis and plaque morphology with fractional flow reserve and outcomes, JAMA Cardiol. 1 (3) (2016) 350–357.

[46] M.D. Griffith, M.C. Thompson, T. Leweke, K. Hourigan, Convective instability in steady stenotic flow: optimal transient growth and experimental observation, J. Fluid Mech. 655 (2010) 504–514.

[47] X. Xie, M. Zheng, D. Wen, Y. Li, S. Xie, A new CFD based non-invasive method for functional diagnosis of coronary stenosis, Biomed. Eng. Online 17 (1) (2018) 36.

[48] G. Ding, K.S. Choi, B. Ma, T. Kato, W. Yuan, Transitional pulsatile flows with stenosis in a two-dimensional channel, Phys. Fluids 33 (3) (2021) 034115.

[49] K. Melih Guleren, Numerical flow analysis of coronary arteries through concentric and eccentric stenosed geometries, J. Biomech. 46 (6) (2013) 1043–1052.

[50] E. Falk, P.K. Shah, V. Fuster, Coronary plaque disruption, Circulation 92 (3) (1995) 657–671.

[51] ANSYS® (version 19.0, Cannonsburg, PA, US), ANSYS® Academic Research Mechanical, Release 19.0, Mechanical APDL Theory Reference, Structures with Material Nonlinearities, Hyperelasticity, Anisotropic Hyperelasticiticy, ANSYS Inc, 2019.

[52] G.A. Holzapfel, G. Sommer, C.T. Gasser, P. Regitnig, Determination of layer-specific mechanical properties of human coronary arteries with nonatherosclerotic intimal thickening and related constitutive modeling, Am. J. Physiol.-Heart Circ. Physiol. 289 (5) (2005) 2048–2058.

[53] A. Schiavone, L.G. Zhao, A computational study of stent performance by considering vessel anisotropy and residual stresses, Mater. Sci. Eng. C 62 (2016) 307–316.

[54] M. Mooney, A theory of large elastic deformation, J. Appl. Phys. 11 (9) (1940) 582–592.

[55] R.S. Rivlin, Large elastic deformations of isotropic materials IV. Further developments of the general theory, Philos. Trans. R. Soc. Lond., Math. Phys. Sci. 241 (835) (1948) 379–397.

[56] A. Versluis, A.J. Bank, W.H. Douglas, Fatigue and plaque rupture in myocardial infarction, J. Biomech. 39 (2) (2006) 339–347.

[57] G.A. Holzapfel, R.W. Ogden, Biomechanics of Soft Tissue in Cardiovascular Systems, 441, Springer, 2014.

[58] A.L. Dalibard, D Gérard-Varet, Effective boundary condition at a rough surface starting from a slip condition, J. Differ. Equ. 251 (12) (2011) 3450–3487.

[59] G.A. Zampogna, J. Magnaudet, A. Bottaro, Generalized slip condition over rough surfaces, J. Fluid Mech. 858 (2019) 407–436.

[60] S. Hina, M. Mustafa, T. Hayat, A. Alsaedi, Peristaltic flow of Powell-Eyring fluid in curved channel with heat transfer: a useful application in biomedicine, Comput. Methods Programs Biomed. 135 (2016) 89–100.

[61] M.L. Rizzini, D. Gallo, G. De Nisco, F. D'Ascenzo, C. Chiastra, P.P. Bocchino, F. Piroli, G.M. De Ferrari, U. Morbiducci, Does the inflow velocity profile influence physiologically relevant flow patterns in computational hemodynamic models of left anterior descending coronary artery? Med. Eng. Phys. 82 (2020) 58–69.

[62] J. Myers, J. Moore, M. Ojha, K. Johnston, C. Ethier, Factors influencing blood flow patterns in the human right coronary artery, Ann. Biomed. Eng. 29 (2) (2001) 109–120.

[63] E. Davies Justin, I. Whinnett Zachary, P. Francis Darrel, H. Manisty Charlotte, J. Aguado-Sierra, K. Willson, A. Foale Rodney, S. Malik Iqbal, D. Hughes Alun, H. Parker Kim, J. Mayet, Evidence of a dominant backward-propagating "suction" wave responsible for diastolic coronary filling in humans, attenuated in left ventricular hypertrophy, Circulation 113 (14) (2006) 1768–1778.

[64] M. Abbasian, M. Shams, Z. Valizadeh, A. Moshfegh, A. Javadzadegan, S. Cheng, Effects of different non-Newtonian models on unsteady blood flow hemodynamics in patient-specific arterial models with in-vivo validation, Comput. Methods Programs Biomed. 186 (2020) 1–15.

[65] L. Könözsy, The k-omega shear-stress transport (SST) turbulence model, in: A New Hypothesis On the Anisotropic Reynolds Stress Tensor For Turbulent Flows, Springer, 2019, pp. 57–66.

[66] A. Mahalingam, U.U. Gawandalkar, G. Kini, A. Buradi, T. Araki, N. Ikeda, A. Nicolaides, J.R. Laird, L. Saba, J.S. Suri, Numerical analysis of the effect of turbulence transition on the hemodynamic parameters in human coronary arteries, Cardiovasc. Diagn. Ther. 6 (3) (2016) 208–220.

[67] F.P.P. Tan, G. Soloperto, S. Bashford, N.B. Wood, S. Thom, A. Hughes, X.Y. Xu, Analysis of flow disturbance in a stenosed carotid artery bifurcation using two-equation transitional and turbulence models, J. Biomech. Eng. 130 (6) (2008).

[68] J. Ryval, A.G. Straatman, D.A. Steinman, Two-equation turbulence modeling of pulsatile flow in a stenosed tube, J. Biomech. Eng. 126 (5) (2004) 625–635.

[69] M.X. Li, J.J. Beech-Brandt, L.R. John, P.R. Hoskins, W.J. Easson, Numerical analysis of pulsatile blood flow and vessel wall mechanics in different degrees of stenoses, J. Biomech. 40 (16) (2007) 3715–3724.

[70] M.A. Kabir, M.F. Alam, M.A. Uddin, Numerical simulation of pulsatile blood flow: a study with normal artery, and arteries with single and multiple stenosis, J. Eng. Appl. Sci. 68 (1) (2021) 24.

[71] S.S. Varghese, S.H. Frankel, Numerical modeling of pulsatile turbulent flow in stenotic vessels, J. Biomech. Eng. 125 (4) (2003) 445–460.

[72] S.K. Shanmugavelayudam, D.A. Rubenstein, W. Yin, Effect of geometrical assumptions on numerical modeling of coronary blood flow under normal and disease conditions, J. Biomech. Eng. 132 (6) (2010).

[73] M.C. Paul, M. Mamun Molla, G. Roditi, Large–eddy simulation of pulsatile blood flow, Med. Eng. Phys. 31 (1) (2009) 153–159.

[74] F. Nicoud, C. Chnafa, J. Siguenza, V. Zmijanovic, S. Mendez, P. Wriggers, T. Lenarz, Large-eddy simulation of turbulence in cardiovascular flows, in: Biomedical Technology: Modeling, Experiments and Simulation, Springer International Publishing: Cham, 2018, pp. 147–167.

[75] B. Yang, C. Liu, W. Zheng, S. Liu, Motion prediction via online instantaneous frequency estimation for vision-based beating heart tracking, Inf. Fusion 35 (2017) 58–67.

[76] M. Sauvée, A. Noce, P. Poignet, J. Triboulet, E. Dombre, Three-dimensional heart motion estimation using endoscopic monocular vision system: from artificial landmarks to texture analysis, Biomed. Signal Process. Control 2 (3) (2007) 199–207.

[77] I. Skalidis Emmanuel, I. Parthenakis Frangiskos, P. Patrianakos Alexandros, I. Hamilos Michael, E. Vardas Panos, Regional coronary flow and contractile reserve in patients with idiopathic dilated cardiomyopathy, J. Am. Coll. Cardiol. 44 (10) (2004) 2027–2032.

[78] M. Prosi, K. Perktold, Z. Ding, M.H. Friedman, Influence of curvature dynamics on pulsatile coronary artery flow in a realistic bifurcation model, J. Biomech. 37 (11) (2004) 1767–1775.

[79] Z. Ding, M.H. Friedman, Dynamics of human coronary arterial motion and its potential role in coronary atherogenesis, J. Biomech. Eng. 122 (5) (2000) 488–492.

[80] J.E. Moore Jr, E.S. Weydahl, A Santamarina, Frequency dependence of dynamic curvature effects on flow through coronary arteries, J. Biomech. Eng. 123 (2) (2001) 129–133.

[81] H. Chen, T. Luo, X. Zhao, X. Lu, Y. Huo, G.S. Kassab, Microstructural constitutive model of active coronary media, Biomaterials 34 (31) (2013) 7575–7583.

[82] D.N. Ku, D.P. Giddens, C.K. Zarins, S. Glagov, Pulsatile flow and atherosclerosis in the human carotid bifurcation. Positive correlation between plaque location and low oscillating shear stress, Arteriosclerosis 5 (3) (1985) 293–302.

[83] H.A. Himburg, D.M. Grzybowski, A.L. Hazel, J.A. LaMack, X.M. Li, M.H. Friedman, Spatial comparison between wall shear stress measures and porcine arterial endothelial permeability, Am. J. Physiol. Heart Circ. Physiol. 286 (5) (2004) H1916–H1922.

[84] V. Mazzi, U. Morbiducci, K. Calò, G. De Nisco, M. Lodi Rizzini, E. Torta, G.C.A. Caridi, C. Chiastra, D. Gallo, Wall shear stress topological skeleton analysis in cardiovascular flows: methods and applications, Mathematics 9 (7) (2021) 720.

[85] A.M. Gambaruto, D.J. Doorly, T. Yamaguchi, Wall shear stress and near-wall convective transport: comparisons with vascular remodelling in a peripheral graft anastomosis, J. Comput. Phys. 229 (14) (2010) 5339–5356.

[86] B. Muha, S. Čanić, Existence of a weak solution to a fluid–elastic structure interaction problem with the Navier slip boundary condition, J. Differ. Equ. 260 (12) (2016) 8550–8589.

[87] W. Wang, W. Wang, S. Li, Detection and classification of critical points in piecewise linear vector fields, J. Vis. 21 (1) (2018) 147–161.

[88] H. Bhatia, A. Gyulassy, H. Wang, P.T. Bremer, V. Pascucci, Robust detection of singularities in vector fields, Topological Methods in Data Analysis and Visualization III, Springer International Publishing, Cham, 2014.

[89] N.J. Montarello, K. Singh, A. Sinhal, D.T.L. Wong, R. Alcock, S. Rajendran, R. Dautov, P. Barlis, S. Patel, S.M. Nidorf, P.L. Thompson, T. Salagaras, J. Butters, N. Nerlekar, G. Di Giovanni, J.L. Ottaway, S.J. Nicholls, P.J. Psaltis, Assessing the impact of colchicine on coronary plaque phenotype after myocardial infarction with optical coherence tomography: rationale and design of the COCOMO-ACS study, Cardiovasc. Drugs Ther. (2021) 1–12.

[90] H.J. Carpenter, M.H. Ghayesh, A.C. Zander, J.L. Ottaway, G. Di Giovanni, S.J. Nicholls, P.J. Psaltis, Optical coherence tomography based biomechanical fluid-structure interaction analysis of coronary atherosclerosis progression, J. Vis. Exp. JoVE 179 (2022) 1–35.

[91] F. Gijsen, Y. Katagiri, P. Barlis, C. Bourantas, C. Collet, U. Coskun, J. Daemen, J. Dijkstra, E. Edelman, P. Evans, K. van der Heiden, R. Hose, B.K. Koo, R. Krams, A. Marsden, F. Migliavacca, Y. Onuma, A. Ooi, E. Poon, H. Samady, P. Stone, K. Takahashi, D. Tang, V. Thondapu, E. Tenekecioglu, L. Timmins, R. Torii, J. Wentzel, P. Serruys, Expert recommendations on the assessment of wall shear stress in human coronary arteries: existing methodologies, technical considerations, and clinical applications, Eur. Heart J. 40 (41) (2019) 3421–3433.

[92] S. Chung, K. Vafai, Effect of the fluid–structure interactions on low-density lipoprotein transport within a multi-layered arterial wall, J. Biomech. 45 (2) (2012) 371–381.

[93] D.G. Owen, T. Schenkel, D.E.T. Shepherd, D.M. Espino, Assessment of surface roughness and blood rheology on local coronary haemodynamics: a multi-scale computational fluid dynamics study, J. R. Soc. Interface 17 (169) (2020) 20200327.

[94] I.J. Rao, K.R. Rajagopal, The effect of the slip boundary condition on the flow of fluids in a channel, Acta Mech. 135 (3) (1999) 113–126.

[95] G.A. Holzapfel, R.W. Ogden, Biomechanical Modelling At the molecular, Cellular and Tissue Levels, 508, Springer ScienceBusiness Media, 2009.

[96] M. Biglarian, M.M. Larimi, H.H. Afrouzi, A. Moshfegh, D. Toghraie, A. Javadzadegan, S. Rostami, Computational investigation of stenosis in curvature of coronary artery within both dynamic and static models, Comput. Methods Programs Biomed. 185 (2020) 105170.

[97] J.S. Stroud, S.A. Berger, D. Saloner, Influence of stenosis morphology on flow through severely stenotic vessels: implications for plaque rupture, J. Biomech. 33 (4) (2000) 443–455.

[98] L. Wei, Q. Chen, Z. Li, Influences of plaque eccentricity and composition on the stent–plaque–artery interaction during stent implantation, Biomech. Model. Mechanobiol. 18 (1) (2019) 45–56.

[99] S.M.J.M. Akherat, M. Kimiaghalam, A numerical investigation on pulsatile blood flow through consecutive axi-symmetric stenosis in coronary artery, in: Proceedings of theASME 2010 10th Biennial Conference on Engineering Systems Design and Analysis, Istanbul, Turkey, 2010.

[100] M. Lodi Rizzini, A. Candreva, C. Chiastra, E. Gallinoro, K. Calò, F. D'Ascenzo, B. De Bruyne, T. Mizukami, C. Collet, D. Gallo, U. Morbiducci, Modelling coronary flows: impact of differently measured inflow boundary conditions on vessel-specific computational hemodynamic profiles, Comput. Methods Programs Biomed. 221 (2022) 106882.

[101] H.J. Carpenter, M.H. Ghayesh, A.C. Zander, J. Li, G. Di Giovanni, P.J. Psaltis, Automated coronary optical coherence tomography feature extraction with application to three-dimensional reconstruction, Tomography 8 (3) (2022) 1307–1349.

[102] R. Gharleghi, N. Chen, A. Sowmya, S. Beier, Towards automated coronary artery segmentation: a systematic review, Comput. Methods Programs Biomed. (2022) 107015.

[103] R. Gharleghi, A. Sowmya, S. Beier, Transient wall shear stress estimation in coronary bifurcations using convolutional neural networks, Comput. Methods Programs Biomed. 225 (2022) 107013.

[104] H. Wienemann, C. Ameskamp, H. Mejía-Rentería, V. Mauri, C. Hohmann, S. Baldus, M. Adam, J. Escaned, M. Halbach, Diagnostic performance of quantitative flow ratio versus fractional flow reserve and resting full-cycle ratio in intermediate coronary lesions, Int. J. Cardiol. 362 (2022) 59–67.